

UNIVERSITY OF OKLAHOMA

GRADUATE COLLEGE

INTERPRETATIONAL VARIATIONS OF SEISMIC ATTRIBUTE ANALYSIS AS
COMPARED WITHIN THE TIME AND DEPTH DOMAINS

A THESIS

SUBMITTED TO THE GRADUATE FACULTY

in partial fulfillment of the requirements for the

Degree of

MASTER OF SCIENCE

By

AHMET MURAT ALYAZ

Norman, Oklahoma

2022

INTERPRETATIONAL VARIATIONS OF SEISMIC ATTRIBUTE ANALYSIS AS
COMPARED WITHIN THE TIME AND DEPTH DOMAINS

A THESIS APPROVED FOR THE
SCHOOL OF GEOSCIENCES

BY THE COMMITTEE CONSISTING OF

Dr. Heather Bedle, Chair

Dr. John D. Pigott

Dr. Brett M. Carpenter

© Copyright by AHMET MURAT ALYAZ 2022

All Rights Reserved.

“Considering that the piano is a research area, its keys as data acquisition lines and notes as seismic records, the composer would be the seismic data processor, and the singer would be the seismic interpreter. It can be concluded from the analogy above, seismic interpretation represents the music as a whole and is the art of imaging subsurface geology.”

Ahmet Murat Alyaz

This thesis is dedicated to my father and first teacher, Kazim Alyaz, who passed away seventeen years ago, and to my family who has always trusted and supported me.

ACKNOWLEDGEMENTS

I would first like to express my sincere thanks to my sponsors, the Turkish Ministry of National Education, and the General Directorate of Mineral Research and Exploration (MTA) for giving me support an opportunity to study at the University of Oklahoma. I am grateful to the Education Attaché of Houston and the staff who have always supported me during my time in the United States. I would extend my gratitude to Harold Kleen Memorial Geology & Geophysics and Paul M. Mershon Jr. for giving me scholarships that made really high contributions to my education.

I would like to extend my deepest gratitude to my advisor Dr. Heather Bedle, for the great contributions, support, and constructive advice during my master's degree. Your energy, positivity, and patience made an extraordinary contribution to me becoming a qualified geoscientist. Your knowledge and experience have significantly increased my academic skills. I also thank New Zealand Petroleum & Minerals for making their database available for academic research.

I would like to extend my appreciation to my committee members, Dr. John D. Pigott and Dr. Brett M. Carpenter, for the great contributions and recommendations that I received especially during the proposal phase. It was an honor to have you on my defense committee.

I would like to give my warmest gratitude to the School of Geosciences for providing me with facilities, laboratories, and advanced technology which made this work possible. I would also thank Rebecca Fay, Ashley N. Tullius, and Leah Moser for their significant efforts and support.

I thank the Subsurface Detective Agency for creating a really useful and positive environment for feedback, recommendations, and discussions. Special thanks to Dr. Kurt J. Marfurt for his invaluable wisdom, advice, and contributions. I would also thank Edimar Perico, Jose Pedro Mora

Ortiz, David Lubo-Robles, Karelia La Marca, Marcus V. R. Maas, and Mario Ballinas for giving me feedback, support, and providing a discussion network.

I am indebted to Dr. Özcan Bektaş who put the first brick into the wall in my career. He made invaluable contributions to my life during my bachelor's degree. I also thank other valuable instructors who taught me the engineering discipline. I thank all my colleagues who made me a better geoscientist.

I am fortunate to have two special persons Dr. Attila Aydemir from The Middle East Technical University and Dr. Gökay Bozkurt from TotalEnergies, who have countless contributions to my life. I am grateful to these distinguished lecturers, geoscientists, and colleagues for mentoring me throughout this journey. I would also extend my gratitude to Bülent Oğuz Kılıç from Kross Jeofizik for teaching me many things about geophysics and his invaluable contributions. I thank Dr. Mustafa Ergun from the Institute of Marine Science and Technology, Dokuz Eylul University. He motivated and supported me to become a qualified geophysicist.

Finally, I am incredibly lucky to have an amazing family and so grateful to them for their endless support.

TABLE OF CONTENTS

ACKNOWLEDGEMENT.....	v
TABLE OF CONTENTS.....	vii
LIST OF TABLES.....	xi
LIST OF FIGURES.....	xii
ABSTRACT.....	xvi
CHAPTER 1: INTRODUCTION.....	1
FUNDAMENTALS.....	1
A BRIEF HISTORY OF SEISMIC ATTRIBUTES USED.....	10
MOTIVATION.....	13
WORKFLOW.....	14
REFERENCES.....	15
CHAPTER 2: SEISMIC ATTRIBUTE ASSISTED ANALYSIS OF THE INTERPRETATIONAL VARIATIONS OVER THE TIME AND DEPTH MIGRATED DATASETS: AN EXAMPLE FROM TARANAKI BASIN, NEW ZEALAND.....	19
ABSTRACT.....	19
INTRODUCTION.....	21
GEOLOGIC SETTING.....	25
Tectonic Framework.....	25

Stratigraphic Framework.....	27
DATA AND METHOD.....	28
Seismic Well Tie.....	32
Seismic Interpretation.....	33
RESULTS.....	38
SEISMIC ATTRIBUTE ANALYSIS.....	38
Geometrical Attributes.....	38
Dip and Azimuth Attributes.....	39
Coherence Attributes.....	41
Curvature Attributes.....	44
Physical Attributes.....	47
Envelope Attribute.....	48
Instantaneous Phase Attribute.....	49
Spectral Decomposition Attribute.....	50
SUMMARY.....	54
DISCUSSIONS.....	55
CONCLUSIONS.....	61
ACKNOWLEDGEMENT.....	63

REFERENCES.....	64
CHAPTER 3: FUTURE WORKS.....	69
APPENDIX A – Unit and ray-tracing differences between the time and depth seismic data.....	72
APPENDIX B – 3D visualization of the horizons carried along the composite line.....	73
APPENDIX C – Interpreted and carried horizons on the composite line and modeled version....	74
APPENDIX D – 3D visualization of the dip magnitude analysis for each fault.....	75
APPENDIX E – 3D visualization of the azimuth analysis for each fault.....	76
APPENDIX F – A zoomed display of the distributary channel comparison with horizon slices extracted from the RMS amplitude attribute.....	77
APPENDIX G – A zoomed display of the sinuous channel comparison with horizon slices extracted from the RMS amplitude attribute.....	78
APPENDIX H – A zoomed display of the meandering channel comparison with horizon slices extracted from the RMS amplitude attribute.....	79
APPENDIX I – Co-rendered instantaneous frequency and the Sobel Filter attribute test.....	80
APPENDIX J – Sweetness attribute test results.....	81
APPENDIX K – Amplitude-frequency spectrums of the time domain channels used in the spectral decomposition attribute test results.....	82

APPENDIX L – Amplitude-frequency spectrums of the depth domain channels used in the spectral decomposition attribute test results.....	83
APPENDIX M – Filter bank displays showing tuned frequencies for the selected channels used in the multispectral coherence analysis in both domains.....	84
APPENDIX N – Multispectral Coherence attribute test results.....	85

LIST OF TABLES

Table 2. 1 – The formation summary observed in Okoki-1 well (PR1495)	30
Table 2. 2 – Identified seismic sequences and their descriptions.....	34
Table 2. 3 – Seismic attribute list used in the study (modified after Roden, 2015; Taner, 1994).	38
Table 2. 4 – The summary of the results for each seismic attribute analysis evaluated on geologic events.....	56

LIST OF FIGURES

Figure 1. 1 - Map of the Taranaki Basin map showing the study area and the locations of all data used. Red rectangle shows the 3-D seismic area, blue dot represents location of Okoki-1 well, and black lines correspond to 2-D lines; TA88-2029 and TA88-2020 colored with yellow (taken from Kumar, 2016).	5
Figure 1. 2 - Structural features of the Taranaki Basin (taken from Knox, 1982). The Toro 3D seismic survey (red rectangle) is located in the Turi Fault Zone.....	7
Figure 1. 3 - Structural subdivisions of Taranaki Basin (take from Knox, 1982). The Toro 3D seismic survey (red rectangle) is located in the Turi Fault Zone.....	8
Figure 1. 4 - Miocene-present stratigraphic framework of Taranaki Basin (modified from King and Thrasher, 1996)	9
Figure 1. 5 - The main workflow diagram followed throughout the research.....	15
Figure 2. 1 – a) Main tectonic setting of New Zealand (left), red rectangle represents the borders of the Taranaki Basin (modified from Bradley and Cubrinovski, 2011). A zoomed version of the red rectangle (right) including all datasets used (modified from Kumar, 2016). Red rectangle shows the 3-D seismic area, blue dot represents location of Okoki-1 well, and black lines correspond to 2-D lines; TA88-2029 and TA88-2020 colored with yellow.....	26
Figure 2. 2 – Cretaceous-Cenozoic stratigraphic framework of Taranaki Basin (modified from King and Thrasher, 1996).	27
Figure 2. 3 - a) Detailed geometric diagram of all datasets used and positions of analyzed faults and channels within the cropped volume, b) location of the Okoki-1 well and the distance between	

the tied 2-D TA88-2029. The primary cropped volume is outlined in green. Each channel location within the main crop is marked by a different colored rectangle and normal faults are numbered from F1 to F4. The created composite line (dashed line) starts with TA-88 2029, then, joins with the TA-88 2020, and extends into the 3D seismic area via inline 1800.....31

Figure 2. 4 - a) Well-to-seismic tie of TA-88 2029 and used logs, b) tied traces showing correlation.....32

Figure 2. 5 - Seismic section with inline 2300 showing interpreted horizons and tracked fault, Fault 1. Dashed white polygon represents the Giant Foresets Formation that is our area of interest for the stratigraphic analyzes.....34

Figure 2. 6 - Comparison of normal faults in both domains. The left section represents the time domain, and the right section corresponds to depth domain. Green arrows indicate the foot walls and yellow arrows shows the hanging wall. It is clearly seen that the faults in depth domain (right) show steeper dips and the reflections are more prominent and for this seismic section (xline 9900) channels (white ellipses) look wider in the depth domain.....36

Figure 2. 7 - Interpretational comparison of channels over the time and depth domains using extracted horizon slices (D, S, and M) from RMS amplitude volumes.....37

Figure 2. 8 - The time slices at the top show variance, dip, and azimuth in the time domain, respectively, from left to right. The depth slices at the bottom show the equivalents of the top ones in the depth domain. Orange and black arrows show faults. The red dashed rectangles depict dip changes in both domains.40

Figure 2. 9 - The Sobel Filter attribute comparison with time and depth slices. a) Trace semblance model for time-domain and d) for the depth domain. The top two (b, c) represents the time domain

and the bottom group (e, f) corresponds to the depth domain equivalents. The same-colored arrows are used to highlight variations in the same part of the stratigraphic events in both domains.....43

Figure 2. 10 - The energy ratio similarity attribute comparison with time and depth slices. a) Trace semblance model for time domain and d) for the depth domain. The top three (b, c) represents the time domain and the bottom group (e, f) corresponds to the depth domain. The same-colored arrows are used to highlight variations in the same channels in both domains.....44

Figure 2. 11 - The comparison of co-rendered the most positive and the most negative curvature attributes on the Matemateaonga horizon. a) the curvature model for the time domain, b) the curvature model for the depth domain, c) the extracted horizon in the time domain, d) the extracted horizon in the depth domain. The black arrows show the faults and green arrows point to the curvature variations between the time and depth-migrated datasets. Assuming that the dip angles of the faults are higher in the depth domain, the radius of the curvature should be smaller compared to the time domain. Therefore, I observed larger curvature in the depth-migrated data.....45

Figure 2. 12 - The comparison of co-rendered the most positive, the most negative curvature, and the energy ratio similarity attributes with time and depth slices. The top two boxes show the expected channel geometry in both domains (Figure 2. 12a shows the time domain and Figure 2. 12b represents the depth domain). The black arrows show the faults.....46

Figure 2. 13 - Comparison of envelope attribute application using horizons slices D and S in both domains. a) the trace model for the time domain, d) the trace model for the depth domain. Channels shown in b and c are in the time domain while e and f in the depth domain. Depth domain data exhibit relatively brighter reflections (white arrows) due to the tuning phenomenon associated with the thin beds occurring when the bed thickness is one-quarter of a wavelength ($\lambda/4$)48

Figure 2. 14 - Instantaneous phase comparison between the time and depth data with time and depth slices. The black arrows indicate changes in phase. Note the different phase in channel edges and faults between Figure 14a and b.....49

Figure 2. 15 - Time slices with seismic amplitude (a-distributary channel, b-sinuuous channel, c-meandering channel) and RGB spectral-decomposition blends (d, e, f). Orange arrows represent the prominent amplitude changes in a, b, and c, and the green arrows indicate corresponding frequencies for the same areas on the spectral decomposition RGB blended time slices for each channel. It is seen that bed thickness variations are clearly highlighted in the time migration data.51

Figure 2. 16 - Depth slices with seismic amplitude (a-distributary channel, b-sinuuous channel, c-meandering channel) and RGB spectral-decomposition blends (d, e, f). Orange arrows represent the prominent amplitude changes in a, b, and c, and the green arrows indicate corresponding frequencies for the same areas on the spectral decomposition RGB blended time slices for each channel. The bed thickness variations are better highlighted in the depth migration data.....53

Figure 2. 17 - Fault dip comparison between the depth-converted PSTM (left) and PSDM datasets. Blue ellipses indicate variations observed on horizons.....60

Figure 2. 18 - The Sobel Filter similarity comparisons between the depth-converted PSTM and PSDM datasets. Red arrows indicate the geometric variations in the distributary channel.....61

ABSTRACT

Migration is one of the crucial data processing steps re-locating the recorded seismic events to their true locations, suppressing the diffractions and thus, providing more accurate imaging of the subsurface. It can be applied in the time or depth domain depending on the geologic characteristics of the study area. The time migration algorithm provides a quality imaging of subsurface geology in the areas characterized by intense faulting and complex geologic structures exhibiting sharp dips. However, since the time migration method assumes only mild lateral velocity variations and provides more vertical rather than lateral resolution, in the presence of high lateral velocity contrasts, this approach distorts the imaging quality by creating false geometric constructions such as fault shadows. Therefore, in such areas, depth migration, which has high lateral resolution and is less sensitive to lateral velocity contrasts, is applied to seismic data. Despite such advantages of the depth migration method, there are geometrical and physical variations that might affect the seismic interpretation of the structural and stratigraphic events like faults and channels between both domains worth studying. To analyze these differences, the Taranaki Basin, offshore New Zealand, which exhibits intense faulting and numerous paleochannels, was selected and the Toro 3-D Seismic Survey containing the pre-stack time (PSTM) and depth (PSDM) datasets were used. Unlike previous studies focused on detecting and removing the pitfalls and artifacts generally occurring after depth conversion of the time data or directly observed in the depth-migrated seismic data and as a result, distorting the imaging of the subsurface, even creating fake structures, this research analyzed the variations affecting seismic interpretation between the PSTM and PSDM datasets by using geometrical, physical, and spectral decomposition attributes. This thesis creates awareness for the interpreters by supplying new insights showing how the interpretation of structural (faults) and stratigraphic elements (channels) are changing geometrically (wide, length,

and depth) or physically (amplitude, phase, and frequency). In addition, this work helps decision-makers avoid the increase in exploration studies, seismic risk assessments and drilling costs that might be caused by misinterpretations of the events. To make a comprehensive comparison, the hypothetical models reflecting the expectations were created for each attribute and both qualitative and quantitative interpretations were provided about the findings. The results of the comparisons indicated that the dip angle of the faults increased significantly, the angle of the channel walls are become steeper and more curved, and bodies formed narrower shapes in the depth-migrated data. The observations also showed that there are amplitude and phase variations within and surroundings of the channels which means different lithologic characteristics between both domains. The multispectral coherence analysis demonstrated frequency variations in the channel edges. Despite many limitations like the lack of borehole data in the 3D area, using only four normal faults and three different types of channels formed in the same formation (the Giant Foresets Formation), this study provides useful results to understand what interpretational variations can lead to.

CHAPTER 1: INTRODUCTION

FUNDAMENTALS

In traditional seismic surveys, seismic signals reflecting from the layer interfaces between rocks possessing different features of properties, are recorded by velocity-distance relation based on the shot and receiver pair geometry as a function of time passed throughout the seismic wave's journey. This results in reflections that are recorded and processed in the time domain using two-way travel time in the beginning. If depth conversion is required, this process is achieved by using well tops corresponding to geological layers in the well, velocities measured in the wells (check-shot survey), quantitative knowledge about rock velocities, and/or Root Mean Square (RMS) stacking velocities which are calculated from seismic data (Etris et al, 2002). Depth conversion is sometimes confused with depth migration, which is a completely different process (Etris et al, 2002), and these differences must be kept in mind. Migration aims to move the dipping reflections to their true subsurface locations, suppresses the diffractions, and eliminates non-hyperbolic move-outs caused by strong lateral velocity variations, and thus, increase the imaging quality (Gazdag and Sguazzero, 1984; Yilmaz, 2001; Etgen and Kumar, 2012). Migration can be applied either before (pre-stack migration) or after (post-stack migration) the stacking process and in both time and depth domains.

The compelling reason for doing migration in the time domain is associated with the dipping events whereas it was related to the strong lateral velocity changes in the depth domain (Yilmaz, 2001). The time migration is used to account for the behavior of the fault plane reflections and reflections within the fault blocks which cause dips clashing with each other in the 3-D seismic data (Yilmaz,

2001). Depth migration with 3-D seismic, on the other hand, is superior in accounting for the complex overburden structures that lead to lateral velocity changes (Yilmaz, 2001). Since the strong velocity variations cause high ray bending at the interfaces, it gives rise to non-hyperbolic behavior of the arriving times on CMP gathers, and because CMP stacking works by assuming hyperbolic moveouts, amplitudes and travel times related to the events are distorted (Rahun-Jain, 2012). Therefore, both time and depth migration algorithms can only provide better imaging of the subsurface when they are applied before the conventional CMP stacking step (Yilmaz, 2001; Rahun-Jain, 2012).

There are distinct types of migration methods (the Kirchhoff, Stolt, and Finite-difference migrations) performed in the time domain seismic data. The prestack Kirchhoff time migration is the most widely used method in conventional image processing due to a relatively lower computation time, the adaptation ability to the irregular topography, and providing the flexibility to output for the selected CMP gathers in their migrated locations (Yilmaz, 2001). In prestack Kirchhoff time migration, the energy (amplitudes) scattered from a subsurface point to all receivers are summed along the traveltimes surface using Kirchhoff diffraction integral, and then, sent to an output migrated location (Bancroft et al, 1998; Yilmaz, 2001). If the subsurface exhibits strong lateral velocity variations that require depth migration, a velocity model that comes from the PSTM is updated by accounting for the topographic characteristics and velocities are converted from the RMS to the interval velocities by Dix's equations. Finally, the output is the prestack Kirchhoff depth migration which provides more accurate imaging with high resolution.

The time migration algorithm assumes straight rays between surface and reflectors and most time-migration algorithms including the Kirchhoff method used to create our datasets use RMS velocity. Furthermore, the time migration algorithm accepts that the velocity is constant both horizontally and vertically (Hill and Rüger, 2019). This assumption creates inaccuracy in the imaging of seismic data in the presence of the strong lateral velocity variations and dipping events due to not accounting for ray bending at interfaces (Hill and Rüger, 2019; Li and Fomel, 2014; Young et al., 2009; Goodway et al., 2016). In contrast, depth migration accounts for ray bending and uses interval velocities and is especially useful in the areas characterized by robust horizontal velocity contrasts such as salt bodies (Hill and Rüger, 2019; Young et al., 2009; Jain, 2012). The depth migration diminishes the Fresnel zone which is a measure of the lateral resolution of the seismic data (Schleicher and Santos, 2001). It is easier to distinguish between two reflecting points when the Fresnel zones are narrower. As a result, the Fresnel-zone width represents the measure of lateral resolution (Yilmaz, 2001). Another fundamental difference I want to mention in this section is the visual definitions of frequency and wavenumber relation between time and depth domains. Time-domain data uses cycle/second (Hertz) for frequency unit in seismic volumes while depth domain is using cycles/km (wavenumber - k) (see Appendix A) (Hill and Rüger, 2019).

Although it is thought that performing depth migration can solve the imaging problems for the data sets suffering from the robust lateral velocity changes, the nature of the algorithm brings its own variations, pitfalls, and disadvantages for the seismic interpretation. Previous studies (Etris et al, 2002; Etgen and Kumar, 2012; Marfurt and Alves, 2015; Lin et al, 2015; Grigorova, 2016; Birdus and Artyomov, 2019) discussed these problems (processing artifacts, multiples, noise, aliasing, and fault shadows) by directly comparing the original seismic time and depth migrated

datasets to each other or using seismic attributes. In this research, unlike the previous studies that are generally related to the differences revealed after depth migration or the application of seismic attributes in the time and depth domains, I focus on their effects on the interpretation of the structural and stratigraphic events by performing a much wider variety of seismic attributes supported by qualitative and quantitative analyses.

The research aims to assist seismic interpreters in gaining insight into the interpretational variations of the structural and stratigraphic events in both domains and present them with a comparative analysis to avoid their potential misinterpretations. For this purpose, the Taranaki Basin which contains excellent examples of faults and channel systems was studied. The Toro 3-D Seismic Survey datasets, which were acquired from the coast of Taranaki Peninsula, New Zealand in 2007, had not previously been used for such a comparative analysis, and the geology of the study area had generally been studied using time datasets.

The Toro 3-D seismic survey contains both prestack time (PSTM) and -depth migrated (PSDM) datasets. However, just like most seismic surveys, the Toro 3D survey lacks borehole data. To correlate the seismic with the borehole data, I used two 2D seismic lines (TA88-2020 and TA88-2029), which are perpendicular to each other, from the TA88 seismic survey which was acquired in 1988. The TA88-2020 seismic line intersects with the TA88-2029 line and crosses through the Toro 3D seismic survey. Well-tie was performed using the TA88-2029 line which is crossing approximately 700 m far from the Okoki-1 well (Fig. 1. 1).

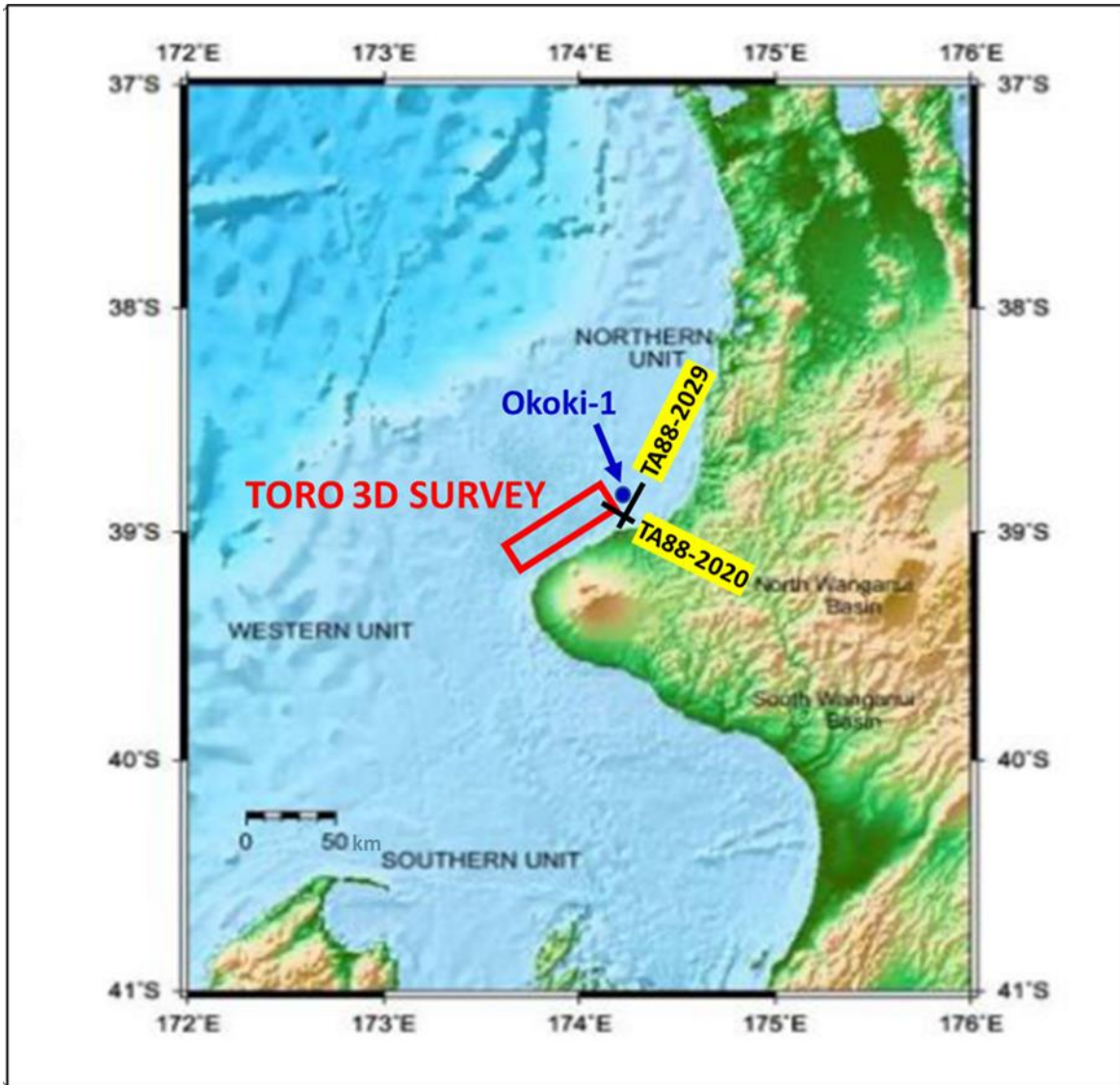


Figure 1. 1: Map of the Taranaki Basin map showing the study area and the locations of all data used. Red rectangle shows the 3-D seismic area, blue dot represents location of Okoki-1 well, and black lines correspond to 2-D lines; TA88-2029 and TA88-2020 colored with yellow (taken from Kumar, 2016).

The Taranaki Basin extends along New Zealand's western coast of the North Island from north to south (Fig. 1. 2), covering an area of approximately 300,000 km² (King & Thrasher, 1996). The

basin boundaries extend to the Wanganui basin in the east and the Tasman Sea in the west (King & Thrasher, 1996). It has complex geomorphology shaped by tectonic events and thus, its geology consists of many sub-basins and uplifts dated between the mid-Cretaceous to the present (King & Thrasher, 1996). Three major tectonic belts, the Taranaki Boundary Fault in the N-S direction, the Cape Egmond Fault Zone lying through the northern and western units of the Taranaki Graben, and the Cook-Turi Fault Zone (Fig. 1. 3), play a key role in forming the geology (King & Thrasher, 1996). The faults selected for the structural variation experiments between both domains are in the Turi Fault Zone.

The primary depositional environment of the Taranaki Basin is divided into four main stratigraphic divisions: 1) Late Cretaceous syn-rift sequence, named as Pakawau Group, 2) Paleocene-Eocene late-rift and post-rift transgressive sequence covering Kapuni and Moa Groups, 3) Oligocene-Miocene foredeep and distal sediment starved shelf and slope sequence, Ngatoro Group, and Wai-iti Group as a Miocene regressive sequence, 4) Plio-Pleistocene regressive sequence that is still ongoing in Rotokare Group (King & Thrasher, 1996). The channels selected for the stratigraphic variation analyses were formed within the Giant Foresets Formation which started to take shape during the last periods of the Wai-iti Group but mostly formed in the Rotakare Group (Fig. 1. 4) whose sedimentary records are dated between the Late Miocene to the present (King & Thrasher, 1996). The detailed information about the structural and stratigraphic frameworks of Taranaki Basin are presented in Chapter 2.

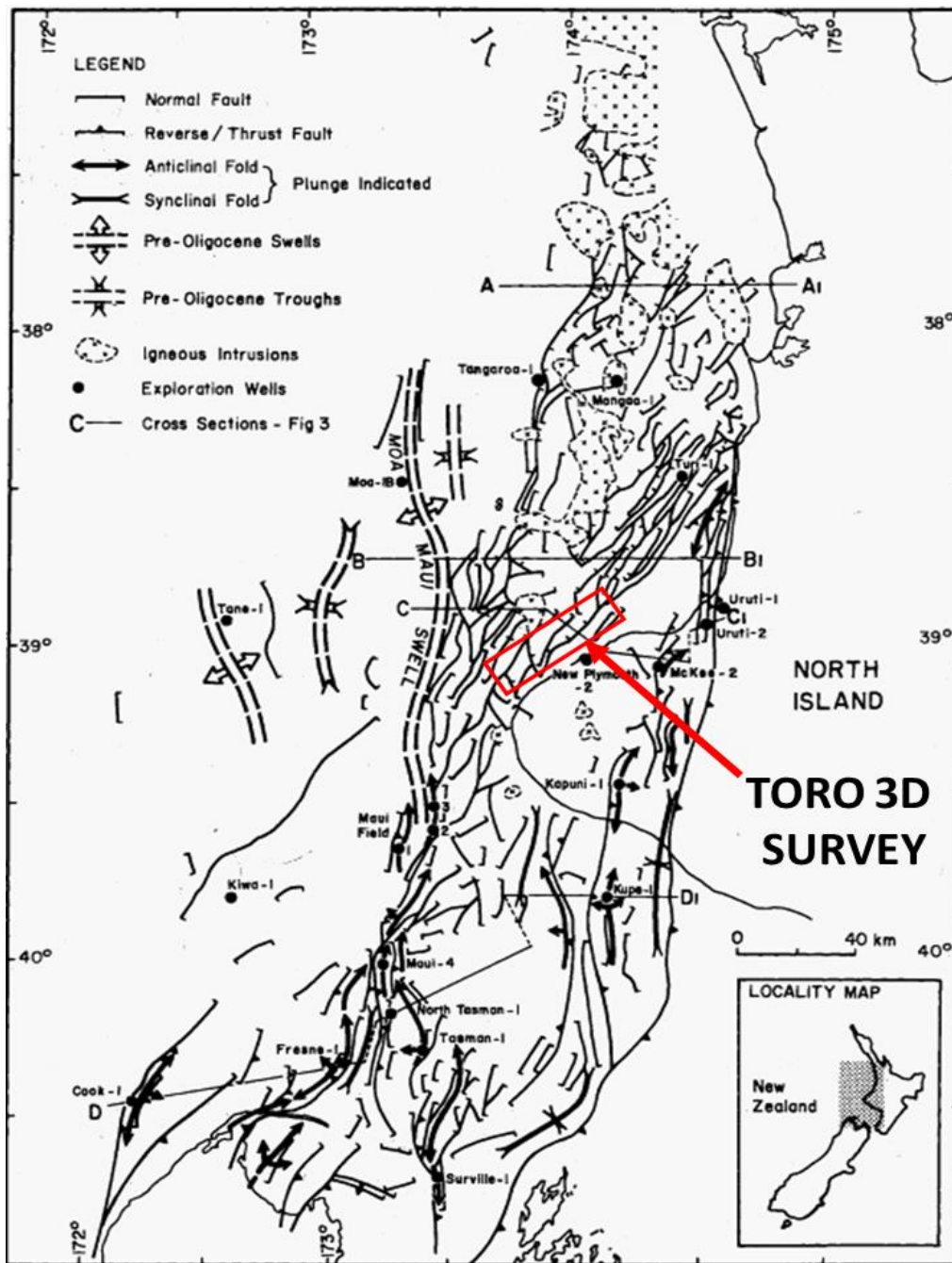


Figure 1. 2: Structural features of the Taranaki Basin (taken from Knox, 1982). The Toro 3D seismic survey (red rectangle) is located in the Turi Fault Zone.

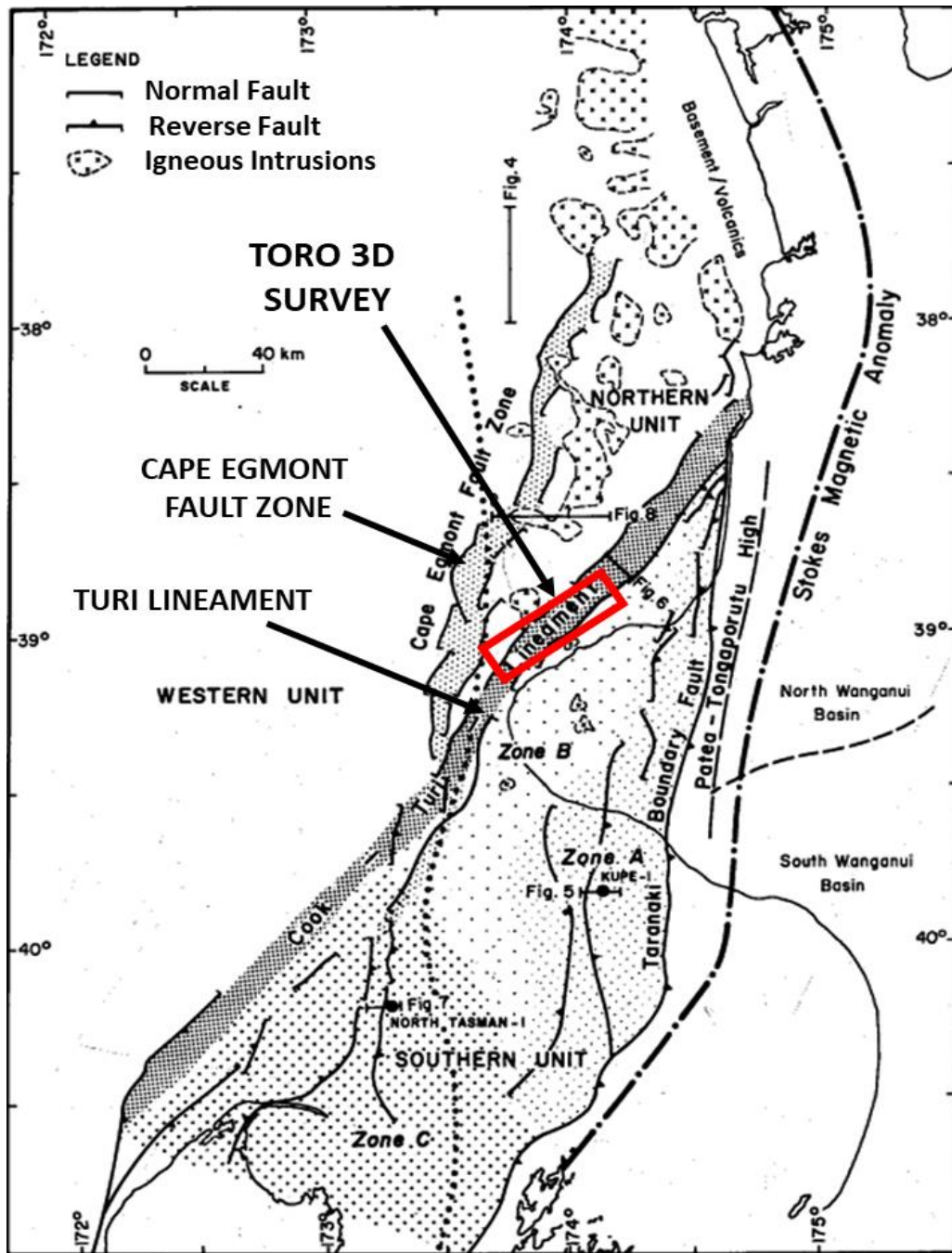


Figure 1. 3: Structural subdivisions of the Taranaki Basin (taken from Knox, 1982). The Toro 3D seismic survey (red rectangle) is located in the Turi Fault Zone.

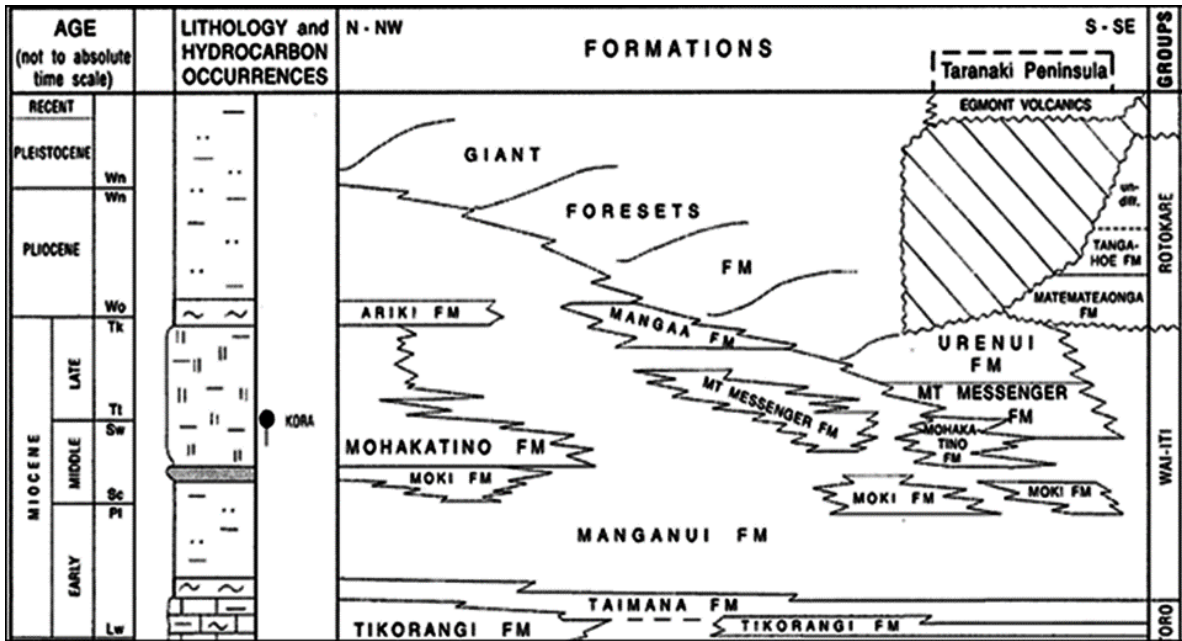


Figure 1. 4: Miocene-present stratigraphic framework of the Taranaki Basin (modified from King and Thrasher, 1996).

During the seismic interpretation phase, four sub-parallel normal faults in the Turi Fault Zone extending in a northeast-southwest direction (Fig. 1. 3), were interpreted in the area. They then numbered from F1 to F4. Dip, azimuth, coherence (the Sobel Filter and energy ratio similarity), variance, and curvature attributes were applied to these faults. Additionally, three distinct types of channels with ages ranging from Miocene to Pliocene (Fig. 1. 4) were selected to perform stratigraphic analysis using an envelope, instantaneous phase, instantaneous frequency, sweetness, spectral decomposition, and multispectral coherence attributes. Coherence (the Sobel Filter and energy ratio similarity) and curvature attributes were used to highlight channel edges as well, and then, co-rendered with the physical attributes. To present a comprehensive analysis showing interpretational variability, both structural and stratigraphic comparisons were examined in both

time and depth-migrated data. The detailed information about the seismic attributes used was provided in the following section.

A BRIEF HISTORY OF SEISMIC ATTRIBUTES USED

From the early 1960s, the advantages provided by rapidly developing technology in computer systems made significant contributions to seismic interpretation and led to the seismic attributes era. Seismic attributes are quantitative information derived from the seismic data and allow geoscientists to analyze features (e.g., amplitude, frequency, phase) that might not be noticed on standard seismograms. Balch's (1971) paper started a new era by displaying seismic data in color for the first time. Following years, in 1971 and 1972, Anstey (1973) published the results of his works on attributes that were using two different variables (normal seismic trace and the modeled version of interval velocity information) in color.

Taner et al. (1979) developed the studies of predecessors and showed that an analytic signal (or complex trace) can be analyzed as real and imaginary parts. According to this, the amplitude of a seismic signal corresponds to the real part, while the imaginary part is calculated by taking its Hilbert transform. This analysis allow for the computation of three seismic attributes that are widely used today: 1) envelope (or reflection strength), which is the square root of the sum of the squares of the real and imaginary parts, 2) phase, which is the inverse tangent of the imaginary and real parts, and 3) frequency, that is the rate of phase change at a given time (Taner et al, 1979).

In the early 1990s, Rijks and Jaufred (1991) placed a plane through the adjacent points and measured the dip angles between them, then, gathered the dip values at the central point relative to a local reference. Lisle (1994) computed how much the curve bending is at a reference point using the Gaussian Curvature (K). This development furthered the studies over bending structures and helped to understand the lateral changes in dip. Bahorich and Farmer (1995) computed coherence coefficients from seismic amplitudes on neighboring traces using a cross-correlation technique. Today, this method is known as the coherence attribute, and it is extremely useful in revealing fault surfaces and channels within the 3-D seismic data which did not show any reflections in the records. Radovich and Oliveros (1998) described another useful attribute, called sweetness, for the stratigraphic interpretation. It is derived by dividing reflection strength (envelope) by the square root of instantaneous frequency.

The analysis of the frequency spectrum of the seismic data to improve the interpretation of the lithology led to birth a new seismic attribute. Greg Partyka (1999) showed that lateral changes in the frequency can be interpreted as an indicator of lithologic or bed thickness variations. He constrained the analysis window with around 100 ms for the targeted area and measured the lateral changes by observing the amplitude spectra for each frequency. This limited analysis window and separated frequency group analysis were then called short window Fourier transform (SWDFT), also known as spectral decomposition (Partyka et al., 1999).

Gao (2013) introduced a new method to overcome the limitations of the seismic amplitude which does not allow the interpretation of structural details. He created a spectral probe by differentiating

the original waveform, then, used a least-square linear regression method between the wavelet model (spectral probe) and data at each sample location to compute correlation coefficients. This method produced a higher resolution image to analyze the structural events in much more detail than the interpreter could not see in the conventional seismic amplitude. Li and Lu (2014) computed coherence from spectral components to increase the signal-to-noise ratio and quantify the discontinuities which are not seen in the broadband data due to the noise contamination and presented the output using RGB color blending. Their method gave rise to understanding not only highlighting the discontinuities but also analyzing at which frequency they occurred. This method is known as multispectral coherence.

In 1994, Taner introduced a simple and understandable classification for seismic attributes by separating them into two main categories: physical and geometrical attributes. Physical attributes are computed from complex traces and used for lithological and reservoir characteristics. Geometrical attributes are obtained from the reflection configurations and continuity and used in the structural and stratigraphic interpretation (Taner et al., 1994). Chopra and Marfurt (2007) define geometric attributes as discontinuity attributes. I used Taner's main attribute category names by adding spectral decomposition. In Chapter 2, more detailed information is provided about each seismic attribute used, and comparative analysis, interpretations, and discussions are presented about the results.

MOTIVATION

The main motivation of this research is to analyze the possible interpretive differences between the two datasets using seismic attributes and to be able to explain the reasons behind them by answering the following basic questions:

- ❖ How exactly are prestack time-and-depth-migrated datasets similar or different from each other? Why?

- ❖ How the variations between the two datasets affect the seismic interpretation of the events?

- ❖ How do these variations affect the decision-making processes about the area of interest?

WORKFLOW

Once all the required datasets, 3D PSTM and -PSDM, 2D PSTM lines, and Okoki-1 borehole data were obtained, I performed well-tie using the TA88-2029 line and Okoki-1 borehole data. It is important to know that there was approximately a 700 m distance between the seismic line and the Okoki-1 well. Although this situation looks a disadvantage, the seismic data and geology were successfully correlated to each other. Then, all major horizons were picked in both domains. Once the interpretations are completed, the seismic attributes were computed for both qualitative and quantitative comparisons and analyses. In addition to the seismic attribute analyzes, I checked both the time and depth velocity cubes to be sure whether the possible different results obtained in the

attribute calculations were related to the varying velocities. Finally, results were compared in both time and depth and concluded with a detailed discussion. Figure 1. 5 demonstrates the workflow containing each step followed in this research. The results of the seismic interpretations and the seismic attribute analyses were presented in Chapter 2 in detail.

The thesis concludes with Chapter 3, which discusses the significance of the findings on a deeper level and suggests what other areas, attributes, and geologic features should be considered when comparing time vs. depth data.

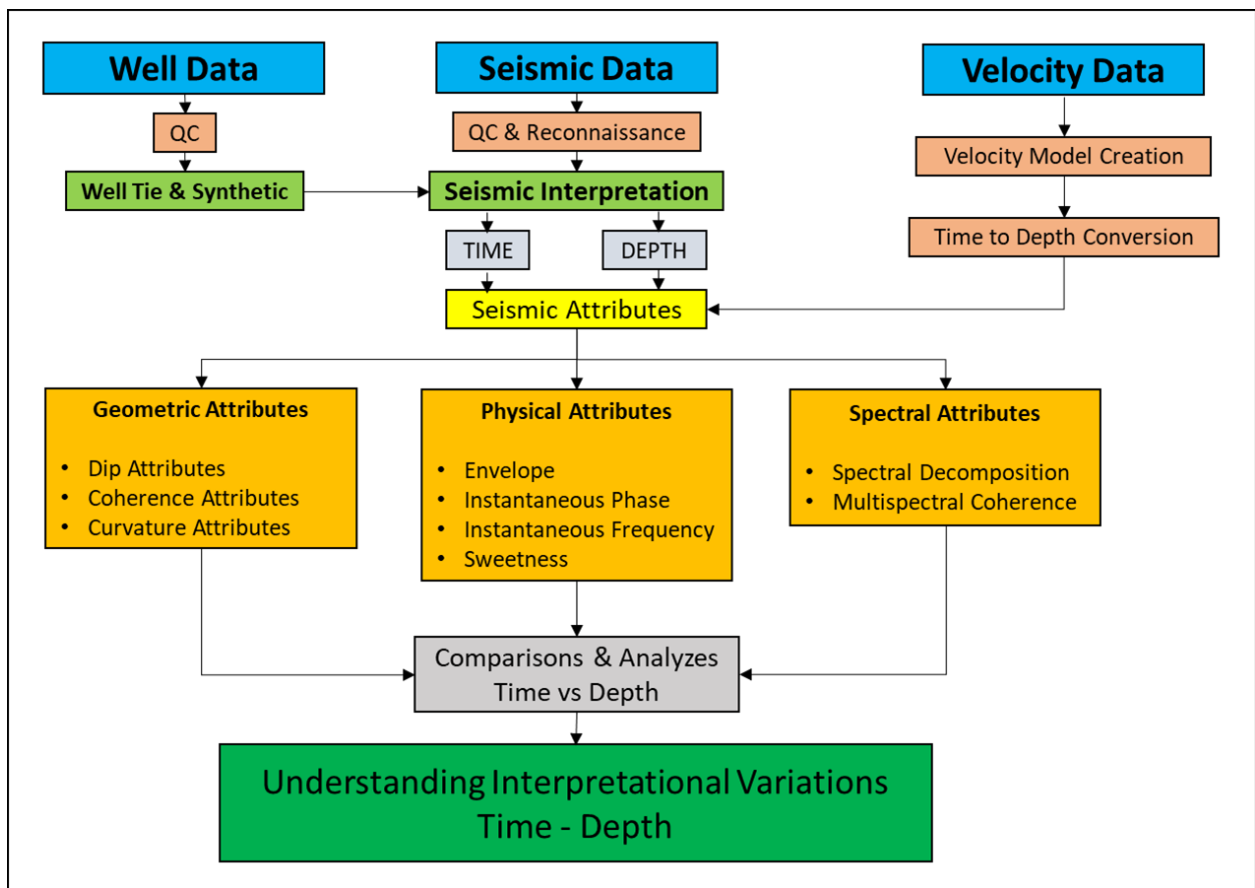


Figure 1. 5: The main workflow diagram followed throughout the research.

REFERENCES

Anstey, N., 1973, The significance of color displays in the direct detection of hydrocarbons: 43rd Annual International Meeting, SEG.

Bahorich, M., and Farmer, S., 1995, 3-D seismic discontinuity for faults and stratigraphic features: The coherence cube: *The Leading Edge* P. 1053-1058.

Balch, A. H., 1971, Color sonograms: A new dimension in seismic data interpretation: *Geophysics* Vol. 36, No. 6 (December 1971), P. 1074-1098, 17 Figs.

Bancroft J. C., Geiger, H. D., Margrave, G. F., 1998, The equivalent offset method of prestack time migration: *Geophysics*, Vol. 63, No.6 (November-December 1998); P. 2042-2053, 16 Figs.

Birdus, S. and Artyomov, A., 2019, Fault shadow distortions on 3D seismic data and their removal by depth processing: *ASEG Extended Abstracts*, 2010:1, 1-4.

Chopra, S., and K. J. Marfurt, 2007, Seismic attributes for prospect identification and reservoir characterization: *SEG Geophysical Development Series*, 11.

Etgen, J. T., and Kumar, C., 2012, What really is the difference between the Time and Depth Migration? A tutorial: *SEG Las Vegas 2012 Annual Meeting*.

Etris, E. L., Crabtree, N. J., and Dewar, J., 2002, True Depth Conversion: More Than a Pretty Picture, *CSEG RECORDER*, Vol. 26, No. 09.

Gao, D., 2013, Wavelet spectral probe for seismic structure interpretation and fracture characterization: A workflow with case studies: *Geophysics*, Vol. 78, No. 5 (September-October 2013); P. O57 – O67, 16 Figs. 10.1190/GEO2012-0427.1

Gazdag, J., and Sguazzero, P., 1984, Migration of Seismic Data: *Proceeding of the IEEE*, Vol. 72, No. 10.

Goodway, B., Purdue, G., Looi, S. Y., Du, L., Rowland, M., 2016, Depth Imaging for Unconventional Reservoir Characterization: Canadian Plains Case Study, GeoConvention 2016, Calgary, Canada.

Grigorova, M., 2016, Comparison between prestack depth migration and direct depth conversion of time migrated section using tomography-based velocity model: 2nd International Scientific Conference GEOBALCANICA 2016.

Hill, S., and Rüger, A., 2019, Illustrated Seismic Processing, Course Notes Series No. 15.

Jain, R., 2012, Kirchhoff Pre-Stack Depth Migration: effective tool for depth imaging: 9th Biennial International Conference & Exposition on Petroleum Geophysics, Hyderabad 2012.

King, P. R., and Thrasher, G. P., 1996, Cretaceous-Cenozoic Geology and Petroleum Systems of the Taranaki Basin, New Zealand: Lower Hutt Institute of Geological & Nuclear Sciences Limited.

Knox, G. J., 1982, Taranaki Basin, structural style and tectonic setting, New Zealand: Journal of Geology and Geophysics, 25:2, 125-140.

Kumar, P. C., 2016, Application of geometric attributes for interpreting faults from seismic data: an example from Taranaki Basin, New Zealand, SEG International Exposition and 86th Annual Meeting, p. 2077-2081.

Li, S. and Fomel, S., 2014, A robust approach to time-to-depth conversion and interval velocity estimation from time migration in the presence of lateral velocity variations: 2014 European Association of Geoscientists & Engineers, Geophysical Prospecting, 63, P. 315–337

Li, F., and Lu, W., 2014, Coherence attribute at different spectral scales: Interpretation, Vol. 2, No. 1 (February 2014); P. SA99 – SA106, 10 Figs.

Lin, T., 2015, Attributes Assisted Seismic Interpretation in Pre-Stack Time versus Depth Migration Data: AAPG Annual Convention & Exhibition 2015, Denver, Colorado, May 31-June 3, 2015.

Lisle, R., 1994, Detection of Zones of Abnormal Strains in Structures Using Gaussian Curvature Analysis: AAPG Bulletin, Vol. 78, No. 12 (December 1994), P, 1811-1819.

Marfurt, K. J., and Alves, T. M., 2015, Pitfalls and limitations in seismic attribute interpretation of tectonic features: Interpretation, Vol. 3, No. 1 (February 2015); P. SB5 – SB15, 10 Figs.

Partyka, G., Gridley, J., and Lopez, J., 1999, Interpretational applications of spectral decomposition in reservoir characterization: The Leading Edge, 18, 353-360.

Radovich, B. J., and Oliveros, R. B., 1998, 3-D sequence interpretation of seismic instantaneous attributes from the Gorgon Field: The Leading Edge 1998.

Rijks, E. J. H., Jauffred, J. C. E. M., 1991, Attribute extraction: An important application in any detailed 3-D interpretation study: Seismic Interpretation 29.

Schleicher J., and Santos, L. T., 2001, Resolution of Kirchhoff depth migration: offset and angle dependence: Annual WIT report 2001.

Taner, M. T., F. Koehler, and R. E. Sheriff, 1979, Complex seismic trace analysis: Geophysics, 44, 1041–1063.

Taner, M. T., Schuelke, J. S., O’Doherty, R., Baysal, E., 1994, Seismic Attributes Revisited: SEG Technical Program Expanded Abstracts 1994.

Yilmaz, O., 2001, Seismic Data Analysis: Processing, Inversion, and Interpretation of Seismic Data: Society of Exploration Geophysicists, Tulsa, OK, 1028 p.

Young, J., Johnson, G., Klug, Stephen., Mathewson, J., 2009, The Case for Depth Imaging All 3D Data: Complex Thrust Belts to Low Relief Resource Plays, WesternGeco; Denver, CO.

CHAPTER 2: SEISMIC ATTRIBUTE ASSISTED ANALYSIS OF THE INTERPRETATIONAL VARIATIONS OVER THE TIME AND DEPTH MIGRATED DATASETS: AN EXAMPLE FROM THE TARANAKI BASIN, NEW ZEALAND

Ahmet Murat Alyaz¹, Heather Bedle¹ and Attila Aydemir^{2,3}

¹University of Oklahoma, Mewbourne College of Earth and Energy, Norman, Oklahoma, U.S.

²METU-NCC, Dept. of Petroleum and Nat. Gas Engineering, Kalkanli, Guzelyurt, Cyprus

³Atilim University, Engineering Faculty, Energy Systems Engineering Dept., Incek, Ankara, Turkey.

Abstract

In the case of complex geology, represented by the dense faulting, folding and dips in the layers, the time migration algorithms provide high-quality imaging for seismic interpretation. However, if there are strong lateral velocity contrasts at the subsurface just like in the onshore Canadian foothills and Irian Jaya (Indonesia), the time migration methods cannot produce satisfactory imaging of the geologic events due to the use of average velocities. Therefore, the depth migration method, which uses interval velocities and assumes that ray-traces indicate bending at interfaces, provides more accurate imaging. Even though the depth migration algorithm has advantages against the time algorithm in complex structures, there are interpretational differences between the time and depth migrated seismic data. To understand these differences, I used the Toro 3D pre-stack time (PSTM) and pre-stack depth migrated (PSDM) datasets acquired from the Taranaki

Basin, offshore New Zealand that consists of numerous structural and stratigraphic complexities, and several seismic attributes have been applied. The comparisons indicate that the dip angle of the faults increased significantly, the angle of the channel levees became steeper and more bend, and structures get narrower in the depth-migrated data. These observations also indicate that there are amplitude and phase variations in and surrounding the channels which means different lithologic characteristics are expected between both domains. It should also be noted that most of the seismic data are in the time domain and there are generally no suitable borehole data and velocity information, and this situation may affect the attribute calculations which give rise to such differences in both domains. This study aims to contribute to a better understanding of the interpretational differences and explain the possible reasons, using some strong attributes that are recently released and widely used in the seismic industry. Previous studies are mainly interested in the improvement of data quality for an easy interpretation with application of some processing steps such as the noise suppression, spectral balance, removal of aliasing, etc. However, the main goal of this investigation is to provide a clear understanding for the interpreters of the possible interpretational differences in the time and depth domains, the reasons behind them, and the connection between the lithology and probable seismic responses by using geometrical and physical attributes. These steps will provide an accurate interpretation and more reliable evaluation of the complex structures.

Keywords: Seismic Attributes; Time vs Depth Migration; Dip and Azimuth; Curvature Attributes; Coherence Attributes; Spectral Decomposition; Taranaki Basin.

Introduction

In conventional seismic surveys, data is always collected in the time domain and subjected to the standard data processing steps. In the usual order of application, there are three primary steps in seismic data processing: deconvolution, stacking and migration (Yilmaz, 2001). Migration is an extremely vital data processing step that moves dipping events to their original subsurface location, suppresses diffractions and eliminates non-hyperbolic move-outs caused by strong lateral velocity variations that directly affect the imaging quality (Gazdag and Sguazzero, 1984; Yilmaz, 2001; Etgen and Kumar, 2012). If the study area exhibits lateral velocity variations, like in the Taranaki Basin, offshore New Zealand (Fig. 2. 1), this situation requires a further step, the depth migration. Therefore, the depth migration is performed using a velocity model created in the time domain to improve the consistency of geological imaging. Although it is considered as a necessary step for better imaging, the interpretational variations between the time and depth-migrated datasets are worth deeper investigations.

Several previous publications (Lin et al, 2015; Etris et al, 2002; Grigorova, 2016; Etgen and Kumar, 2012; Marfurt and Alves, 2005) discuss the differences (processing artifacts, multiples, noises, aliasing, and fault shadows) coming from the nature of data processing in both domains. These studies focused on improving the imaging quality or providing better data by suppressing the noise, spectral balancing of the data, removing the migration-based aliasing effects more than analyzing their effects on imaging. This work broadens the scope of variation analysis by presenting comprehensive comparisons supported by seismic attributes for both spatial and spectral features of the structural and stratigraphic events. Our motivation is to understand the cause-and-effect relationship of the prominent differences or similarities in the seismic

interpretations of structural and stratigraphic features in time and depth domains by using an attribute-assisted workflow. The study aims to assist seismic interpreters in gaining insight into fault and channel interpretation in both domains and avoiding potential misinterpretations. The Toro 3D Seismic Survey datasets, which were acquired from the coast of Taranaki Peninsula, New Zealand in 2007, have not previously been used for such a comparative analysis, and the geology of the study area had generally been studied using only time-domain datasets. To achieve the goal of this investigation, I used both 3D prestack migration datasets. However, since there is no available well data within the 3D area, I used two 2D PSTM lines crossing through the Toro Survey and Okoki-1 well, to correlate seismic with the borehole data (see Fig. 2. 1).

After the discovery of seismic attributes, they were developed and diversified since the early 1970s, and they have gained remarkable popularity having a powerful function on seismic interpretation (Taner et al., 1994). From those times to the present, the perception of seismic attribute use has shifted dramatically, from a qualitative tool to an essential quantitative tool in interpretation (Taner et al., 1994). In 1994, Taner introduced a simple and understandable classification for seismic attributes by separating them into two main categories: physical and geometrical attributes. Physical attributes are computed from complex traces and used for lithological and reservoir characterization. Geometrical attributes are obtained from the reflection configurations and used in the structural and stratigraphic interpretation (Taner et al., 1994). Chopra and Marfurt (2007) re-defined the geometric attributes as discontinuity attributes. Our study follows Taner's (1994) main attribute category names by adding short window discrete Fourier transform (SWDFT) analysis, also known as spectral decomposition, developed by Partyka et al., (1990).

In fault interpretation, to calculate the dip magnitude, Rijks and Jaufred (1991) placed a plane through the adjacent data points and measured the dip angles between them, then, gathered the calculated values at the central point relative to a local reference. To detect the discontinuities at the subsurface, Bahorich and Farmer (1995) presented a method based on computing coherence coefficients from seismic amplitudes on neighboring traces (only three traces) using a cross-correlation technique. Then, Marfurt (1998) generalized their method using the arbitrary number of traces and called this innovative approach multi-trace semblance-based coherence. The coherence attribute is used to highlight faults, buried deltas, channels. Luo et al. (1996) adapted an extremely popular photo enhancement tool, the Sobel Filter, from digital cameras to seismic data for edge detection. This development increased the interpretation quality for faults, channel edges, and fractures. In 2007, Chopra and Marfurt introduced another seismic attribute, energy ratio similarity. It is simply defined as the ratio between coherence and the sum of the energy of the traces used in the analysis window.

Lisle (1994) showed the usefulness of Gaussian Curvature (K) on the calculation curvedness of a given structure. The method simply works by measuring how much the curve bending is relative to a reference point. Then, Roberts (2001) set the inline and crossline coefficients of Lisle's equations to zero and created the most positive and most negative curvature attributes. Taner et al., (1979) analyzed a seismic trace as real and imaginary parts, and then, empirically defined instantaneous amplitude (also known as envelope), instantaneous phase, and instantaneous frequency components of the signal. These components made enormous contributions to understanding the lithologic variations in the area of interest. After the 1990s, Greg Partyka

showed that the variations in the lithology and bed thickness created lateral contrasts in the frequency component of a given seismic signal. He created a time window vertically limited for a time period and analyzed the amplitude-frequency relationship by separating the data into desired frequencies. As it is understood from the limited window and separated frequencies, this method is called short window discrete Fourier Transform (SWDFT) or with its commonly known name: spectral decomposition.

Under the context of geometrical attributes, analyses start with variance, dip, and azimuth calculations to understand the characteristics of four normal faults interpreted in the Turi Fault Zone. Then, it continues to compute energy ratio similarity, Sobel filter, to highlight the geometric characteristics of three different type channels observed in the Giant Foresets Formation (Fig. 2. 2). I also employed the curvature attributes co-rendering the most positive and most negative curvature to compare the variations of the fault characteristics on an extracted horizon. Next, curvature attributes were used by co-rendering with energy ratio similarity on one of the channels for stratigraphic analysis. After that, to understand the lithological differences or similarities, the physical attributes were implemented using the envelope and instantaneous phase, respectively. The last attribute analysis of this study is the application of spectral decomposition used frequency/wavenumber-time relationship. In the end, the research concludes with discussions and conclusions over the observed results.

Geologic Setting

Tectonic Framework

The Taranaki Basin lies throughout the western coast of New Zealand from the north offshore to South (Fig. 2. 1) and covers approximately an area of 300,000 km² (King & Thrasher, 1996). In addition, its boundary starts from the Wanganui Basin in the east and expands into the Tasman Sea (King & Thrasher, 1996). The basin is largely an offshore basin and underlies the continental shelf of the North Island (Thrasher, 1992). The Taranaki Basin has a complex morphology formed by different tectonic events and due to the effects of those conditions, it consists of many sub-basins and uplifts dated from the mid-Cretaceous to the present (King & Thrasher, 1996). Each part has different deformation history throughout the geologic time.

The basin can be structurally defined by the two main parts: the Taranaki Graben and the Western Platform (Pilaar & Wakefield, 1978). The Taranaki Graben is separated into three main directional sectors (northern, western, and southern sections) by tectonic belts (Knox, 1982). These lineaments are the Taranaki Boundary Fault in the N-S direction, the Cape Egmont Fault Zone lying through the northern and the western unit, and the Cook-Turi Fault Zone (Knox, 1978; King & Thrasher, 1996).

The Turi Fault Zone consists of many sub-parallel normal faults dipping into the northwest direction while the Cape Egmond Fault Zone sub-parallel normal faults dipping into eastward (King & Thrasher, 1996). The Cape Egmond Fault Zone is associated with the Miocene extension-related subsidence which is still active in present (Cameron, 2016). Tectonic subsidence made the

Northern Graben remain at a depth of approximately 500 m or deeper than the rest of the Taranaki Basin. This structural form triggered rapid sedimentation (Cameron, 2016). However, uplift on the Turi Fault Zone created a barrier for the sediment provenance from the east (Hansen and Kamp, 2001). Figure 2. 1 shows the main the tectonic frame of the New Zealand and the locations of all datasets used in the Taranaki Basin.

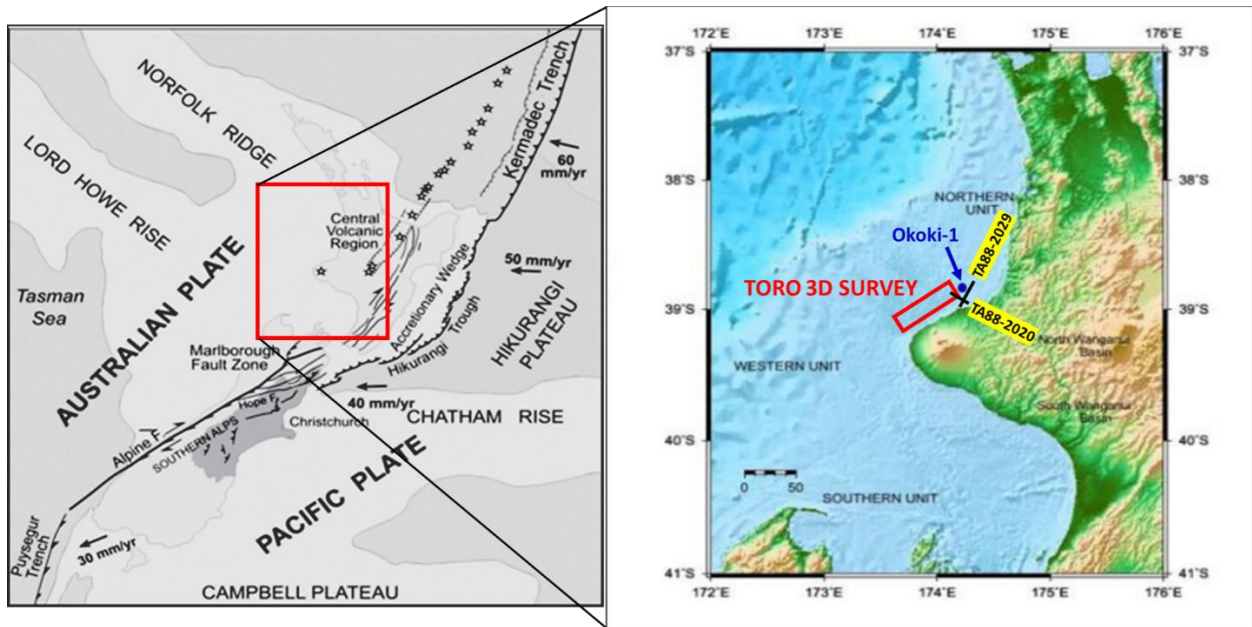


Figure 2. 1: Main tectonic setting of New Zealand (left), red rectangle represents the borders of the Taranaki Basin (modified from Bradley and Cubrinovski, 2011). A zoomed version of the red rectangle (right) including all datasets used (modified from Kumar, 2016). Red rectangle shows the 3-D seismic area, blue dot represents location of Okoki-1 well, and black lines correspond to 2-D lines; TA88-2029 and TA88-2020 colored with yellow.

Stratigraphic Framework

Sedimentary records taken from the Taranaki Basin can be dated between the Early Cretaceous and recent as a major depositional cycle divided into four main stratigraphic subdivisions: 1) Late Cretaceous syn-rift sequence, named as Pakawau Group, 2) Paleocene-Eocene late-rift and post-rift transgressive sequence covering Kapuni and Moa Groups, 3) Oligocene-Miocene foredeep and distal sediment starved shelf and slope sequence, Ngatoro Group, and Wai-iti Group as a Miocene regressive sequence, 4) Plio-Pleistocene regressive sequence that is still ongoing in Rotokare Group (King and Thrasher, 1996). Figure 2. 2 shows the stratigraphic framework from Miocene to the present covering the most related formations in the study.

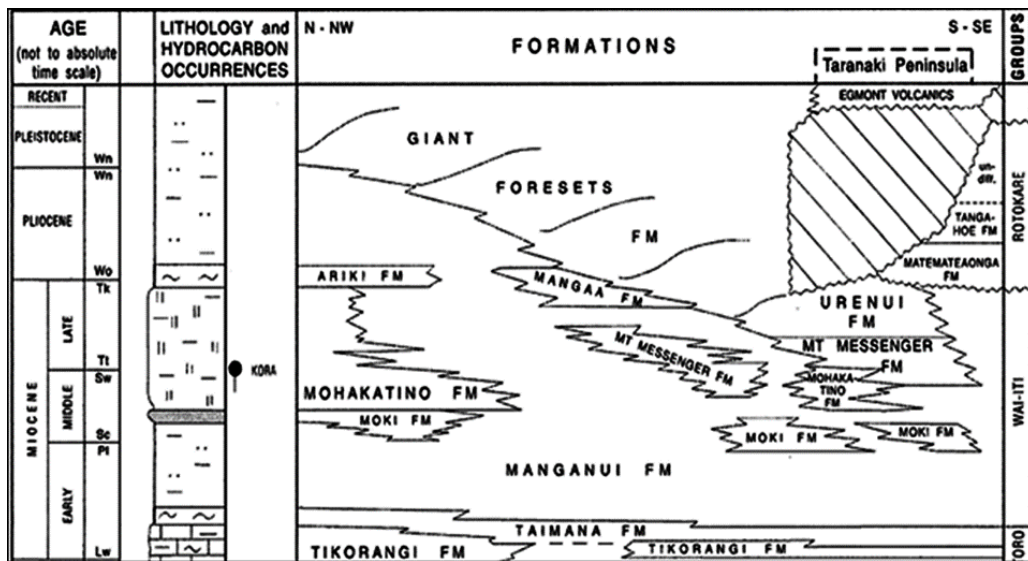


Figure 2. 2: Miocene-present stratigraphic framework of the Taranaki Basin (modified from King and Thrasher, 1996).

The Giant Foresets Formation, which contains mostly fine-grained Plio-Pleistocene deposits and covers the northern and western parts of the Taranaki Basin, began to form in the Late Miocene

and is part of an ongoing regressive sequence (King and Thrasher, 1996). Its depositional environment changes from shelf and slope to the basin floor by siltstone, mudstone, and interspersed sandstones (Hansen and Kamp, 2001). The erosion is the reason for the sediment accumulation eastward (Hansen and Kamp, 2001). The shallowing sea level caused more basinward progradation and increased the sediment flow into deeper section (King and Thrasher, 1996).

Data and Methods

Toro 3D Seismic (with the report code PR3741) is a marine survey and was acquired by Pogo New Zealand in 2007 on the west coast of the north island, New Zealand. It is located in the area of the North Taranaki Basin, covering approximately 150 km² (Fig. 2. 3). The data was acquired with two towed 6000 meters long streamers, the record length is 6 s, and the sample rate is 2 ms then resampled to 4 ms. Bin size of the survey is 12.5 x 25 m. The projection datum used in this survey is NZGD49, then, it was converted to NZGD2000 that I used in the study. Impedance increase at an interface is white (trough) and expressed with negative numbers in the seismic volumes.

According to the seismic processing report (PR3741), the Kirchhoff Prestack Time Migration algorithm using the ray-tracing travel time method was applied to the data. This method migrates the data using X and Y locations to improve the accuracy of subsurface imaging. The set migration aperture was 4 km. During the depth migration, the velocity model was built using the Residual Curvature Analysis (RCA) technique. It employs reflection tomography and was applied with three iterations to update the initial gridded velocity model. The full volume PSDM was obtained as an output.

The TA88 2D seismic survey (PR4436) was conducted by Greymouth Petroleum and submitted to the New Zealand government in 1988. Two different 2D lines from this project, TA88-2029 and 2020, are perpendicular to each other. TA88-2029 is the nearest 2D seismic line to the Okoki-1 well that was provided for this study and TA88-2020 intersects 2029 line and extends into the Toro 3D area (Fig. 2. 3). According to the processing report, the record length is 5 s. Source and receiver intervals are 25 x 25 m and sampling interval is 2 ms. The projection datum is the same as the Toro 3D survey.

There is no drilled well in the Toro 3D area. Thus, to perform the well-tie, Okoki-1 well (Fig. 2. 3) drilled by TCPL Resources Ltd. in 1989 to a total depth (TD) of 4257 m was used. This well data includes a report with lithological definitions, Table 2. 1, and a check-shot data which ensure the time-depth correlation with the seismic data and is only used for picking the major horizons of the formations in the 3D area. The target interval of interest is in the Giant Foresets Formation (Toro 3D Seismic interpretation report) which is younger than the Matemateaonga Formation, represented in Okoki-1 borehole data.

Table 2. 1: Formation table observed in Okoki-1 well (PR1495 well summary report).

Group/Formation	Top (m)	Base (m)	General Lithology
Matemateaonga	70	760	Interbedded sandstones and siltstones with rare shelly conglomerates and claystones.
Urenui	760	1205	Massive interbedded claystones and siltstones.
Mount Messenger - Mohakatino	1205	1811	Massive claystones with minor interbeds of siltstone and tuffaceous sandstone.
Moki	1811	2007	Interbedded sandstones, siltstone and claystone.
Manganui	2007	3434	Massive claystones with minor interbeds of siltstone, sandstone and rare limestone stringers.
Taimana-Otaraoa	3434	3568	Massive calcareous claystones overlying a basal glauconitic sandstone.
Turi	3568	3878	Interbeds of claystone and siltstone with rare sandstone.
Kapuni	3878	4257.5 (TD)	Sandstone interbedded with claystone and siltstone.

Figure 2. 3a shows all the data used along with their locations in detail and Figure2. 3b indicates the distance between the Okoki-1 well and the tied seismic line. Additionally, it displays the elongations of faults and channels selected for analysis. The 3D seismic volume was cropped to include all structural and stratigraphic features to be focused.

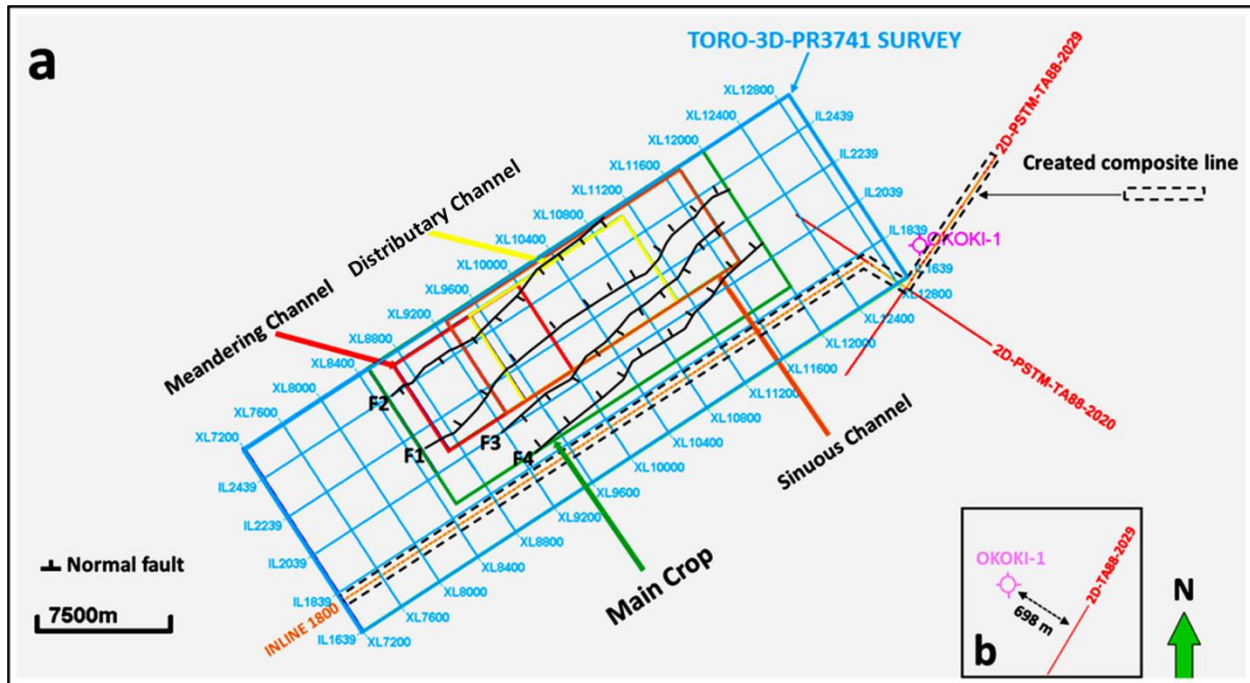


Figure 2. 3: a) Detailed geometric diagram of all datasets used and positions of analyzed faults and channels within the cropped volume, b) location of the Okoki-1 well and the distance between the tied 2-D TA88-2029. The primary cropped volume is outlined in green. Each channel location within the main crop is marked by a different colored rectangle and normal faults are numbered from F1 to F4. The created composite line (dashed line) starts with TA88-2029, then, joins with the TA88-2020, and extends into the 3D seismic area via inline 1800.

Seismic Well-tie

A well-tie was performed by using a zero-phase wavelet, called TORO, with a 21 Hz dominant frequency extracted from the 2D TA88-2029 seismic line. Figure 2. 4a shows logs (DTC, DENS, and GR from left to right) used and created synthetic seismogram. Figure 2. 4b is the trace display to show the well correlation with TA88-2029 seismic section.

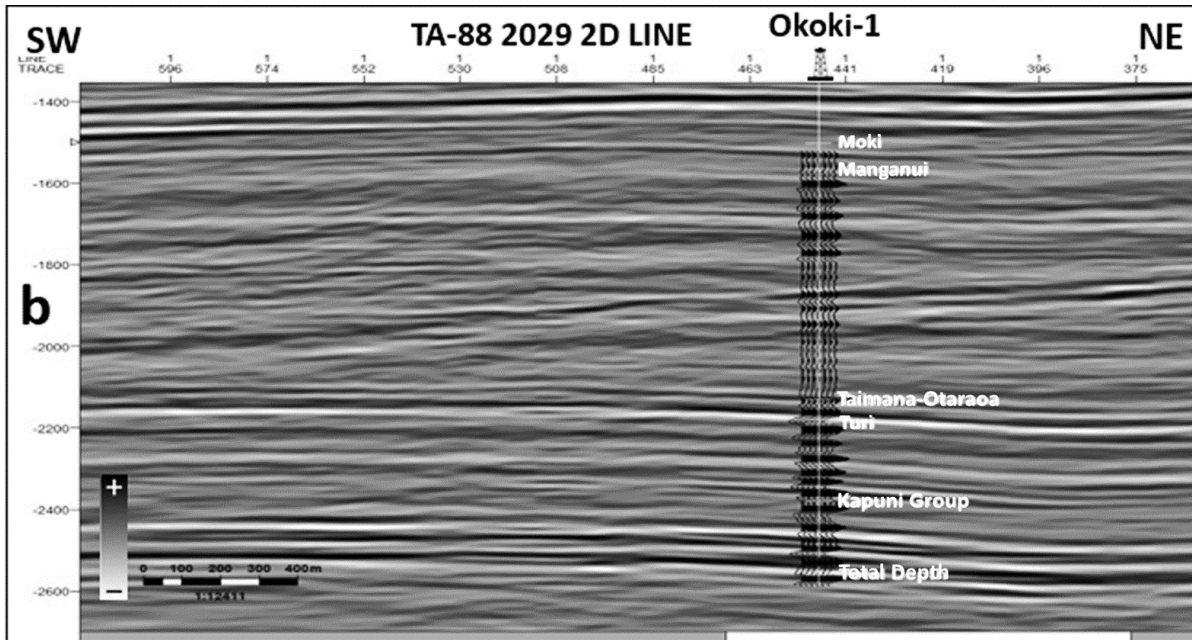
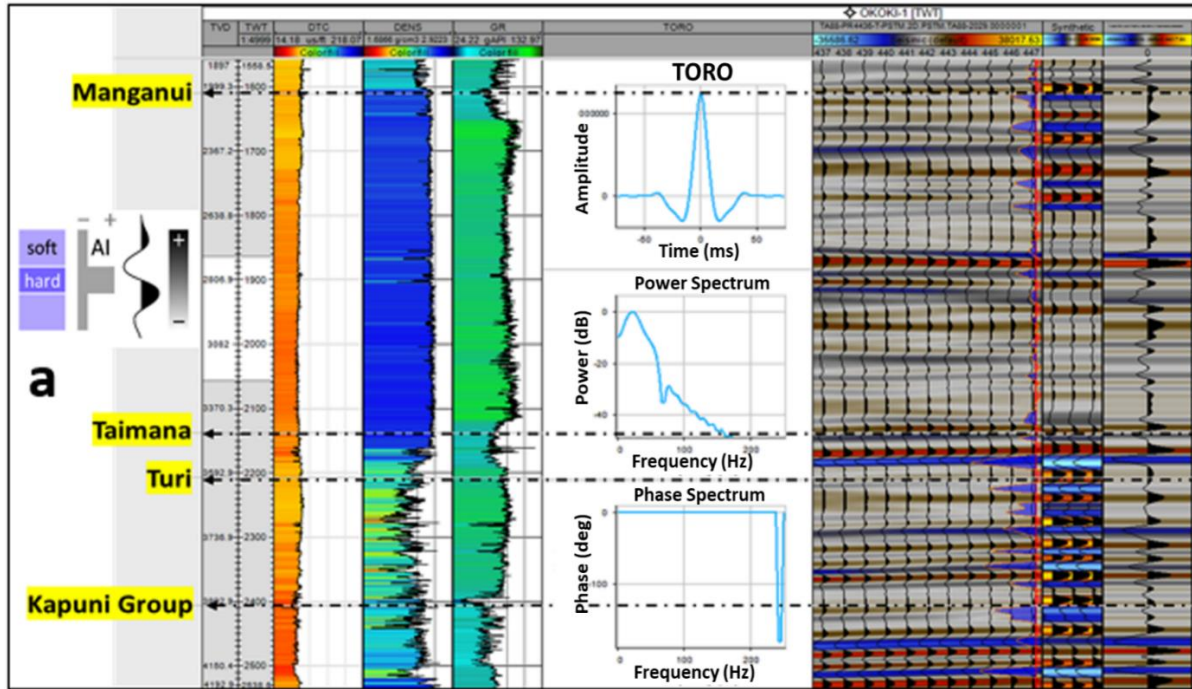


Figure 2. 4: a) Well-to-seismic tie of TA88-2029 and used logs, b) tied traces showing correlation.

Seismic Interpretation

Once the well-tie step is done, the QC check is performed to understand the data quality by checking the amplitude, frequency, and resolution of the data. All horizons were picked with the guidance of formation tops on the TA88-2029 2D line and carried them to the 3D area (see Appendix B for the 3D visualization of the composite line), then, created a model (see Appendix C). Picking was completed in every 25 inline and crosslines starting from the oldest (Kapuni Group) to the youngest (Matemateaonga) formation. Figure 2. 5 illustrates horizon and fault interpretations on the inline 2300 seismic section as an example and Table 2. 2 shows the identified seismic facies.

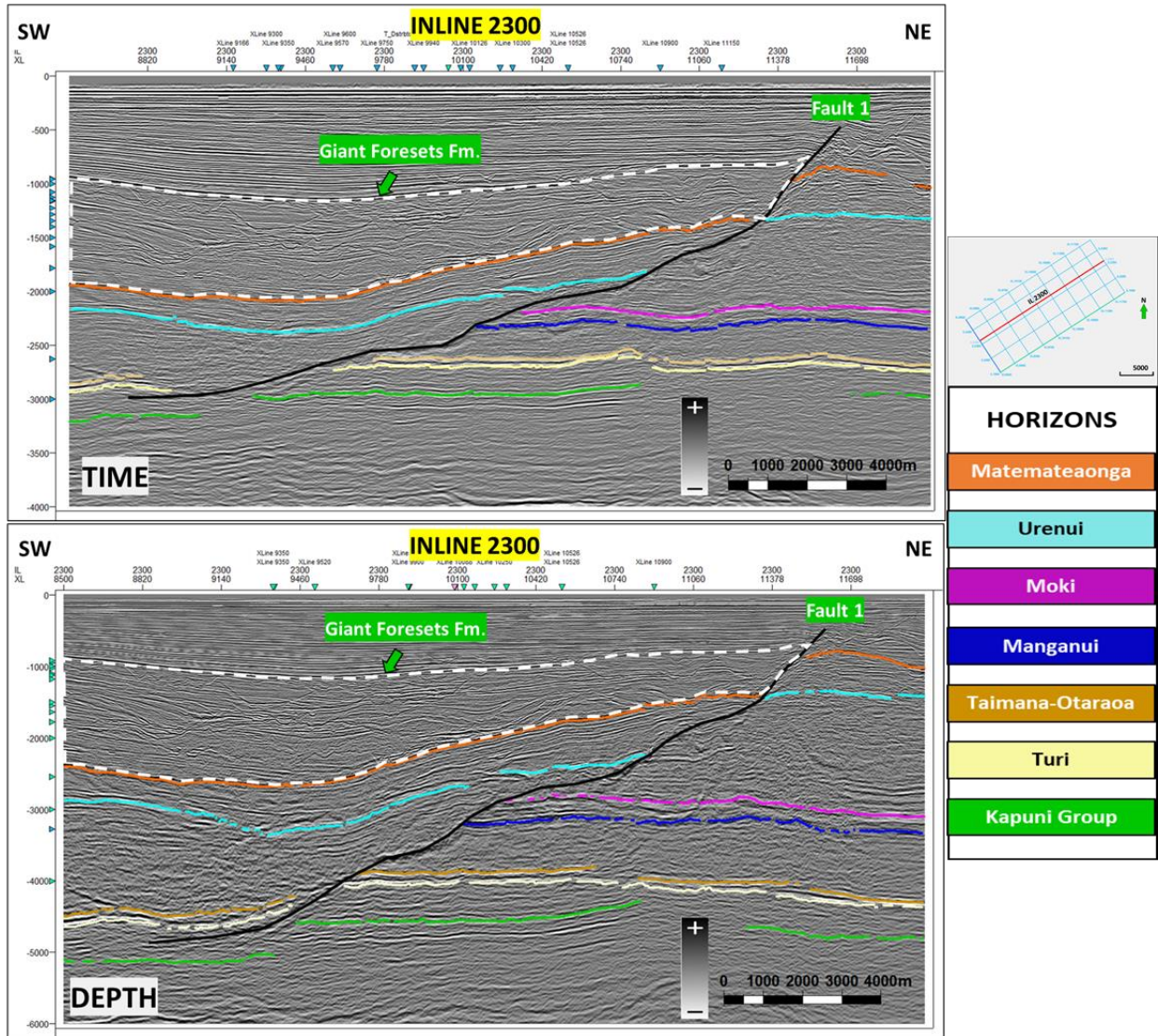
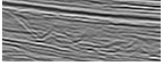
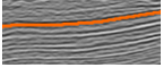
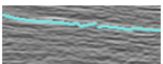
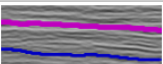
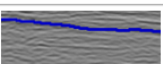
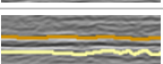




Figure 2. 5: Seismic section with inline 2300 showing interpreted horizons and tracked fault, Fault 1. Dashed white polygon represents the Giant Foresets Formation that is our area of interest for the stratigraphic analyzes.

Table 2. 2: Identified seismic sequences and their descriptions. The colored lines represent the horizons picked at top of each formation.

Seismic Pattern	Formation Name	Age	Interpretation
	Giant Foresets	Early Pliocene-recent	Complex stratified, deformed configuration of high amplitude trend
	Matemateaonga	Late Miocene-Early Pliocene	Parallel reflections of continuous reflections, high amplitude with wavy configuration
	Urenui	Late Miocene-Early Pliocene	Hummocky characteristics of moderate amplitude
	Moki	Early Miocene-Mid-Miocene	Parallel to sub parallel reflections of low amplitude trend
	Manganui	Early Miocene-Early Pliocene	It is identified with a low amplitude of hummocky configuration.
	Taimana-Otaraoa	Early Oligocene-Early Miocene	Formation couple has high amplitude characteristics with the continuous trend and has a sub-parallel reflection configuration.
	Turi	Eocene	The Formation shows a moderate amplitude trend with wavy continuity at the reflections.
	Kapuni Group	Early Paleocene-Late Eocene	It is characterized by variable amplitude in general, has relatively a wavy continuity, and exhibits sub parallel reflections.

All of the interpreted faults (Fault 1, Fault 2, Fault 3, Fault 4) lie in a northeast-southwest direction and pass through the cropped area (Fig. 2. 3). Figure 2. 6 depicts fault tracking across both domains. All four normal faults depicted on crossline 9900 become steeper in the depth domain (right). Additionally, reflections are brighter in the shallow sections of the time domain due to high frequencies. The depth domain, on the other hand, exhibits more prominent reflections at the deeper part of the data due to the depth migration algorithm's lateral resolution advantage.

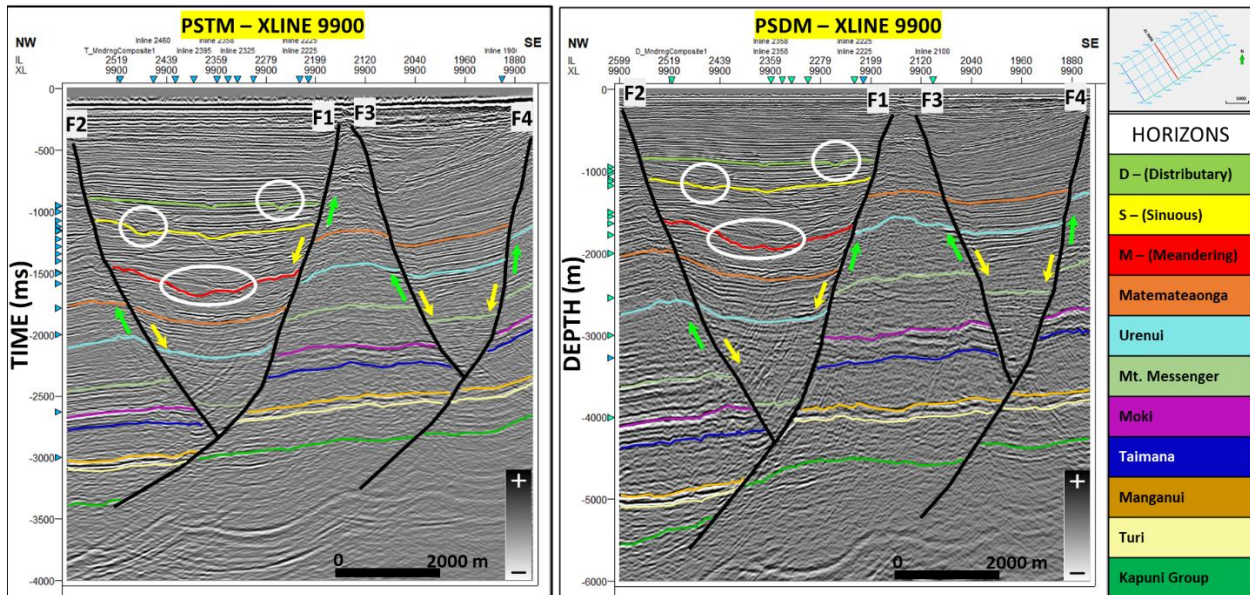


Figure 2. 6: Comparison of normal faults in both domains. The left section represents the time domain, and the right section corresponds to depth domain. Green arrows indicate the foot walls and yellow arrows shows the hanging wall. It is clearly seen that the faults in depth domain (right) show steeper dips and the reflections are more prominent and for this seismic section (xline 9900) channels (white ellipses) look wider in the depth domain.

During the stratigraphic interpretation phase, three channel types within the Giant Foresets Formation with varying geometric characteristics, depositional settings, and buried depths were chosen. Then, three new horizons were interpreted within the Giant Foresets Formation: horizon D (~850 ms above the Matemateaonga Formation) for the distributary channel, horizon S (~650 ms above the Matemateaonga Formation) for the sinuous channel, and horizon M (~300 ms above the Matemateaonga Formation) for the meandering channel (Fig. 2. 6). In the time domain, their depths range from 900 ms to 1700 ms, while they range from 850 m to 2000 m in the depth domain. Figure 2. 7 depicts the seismic interpretations of all three channels studied. Blue circles represent

the prominent differences. The distributary channel in depth domain clearly shows a better appearance with its branches on the vertical seismic cross-section because of the higher lateral resolution. Channels appear wider and flatter on the vertical seismic section in the time domain whereas they exhibited a narrower shape, and their edges look steeper in the depth domain (Fig. 2. 7). The zoomed versions of these comparisons are provided in Appendices – F, G, H.

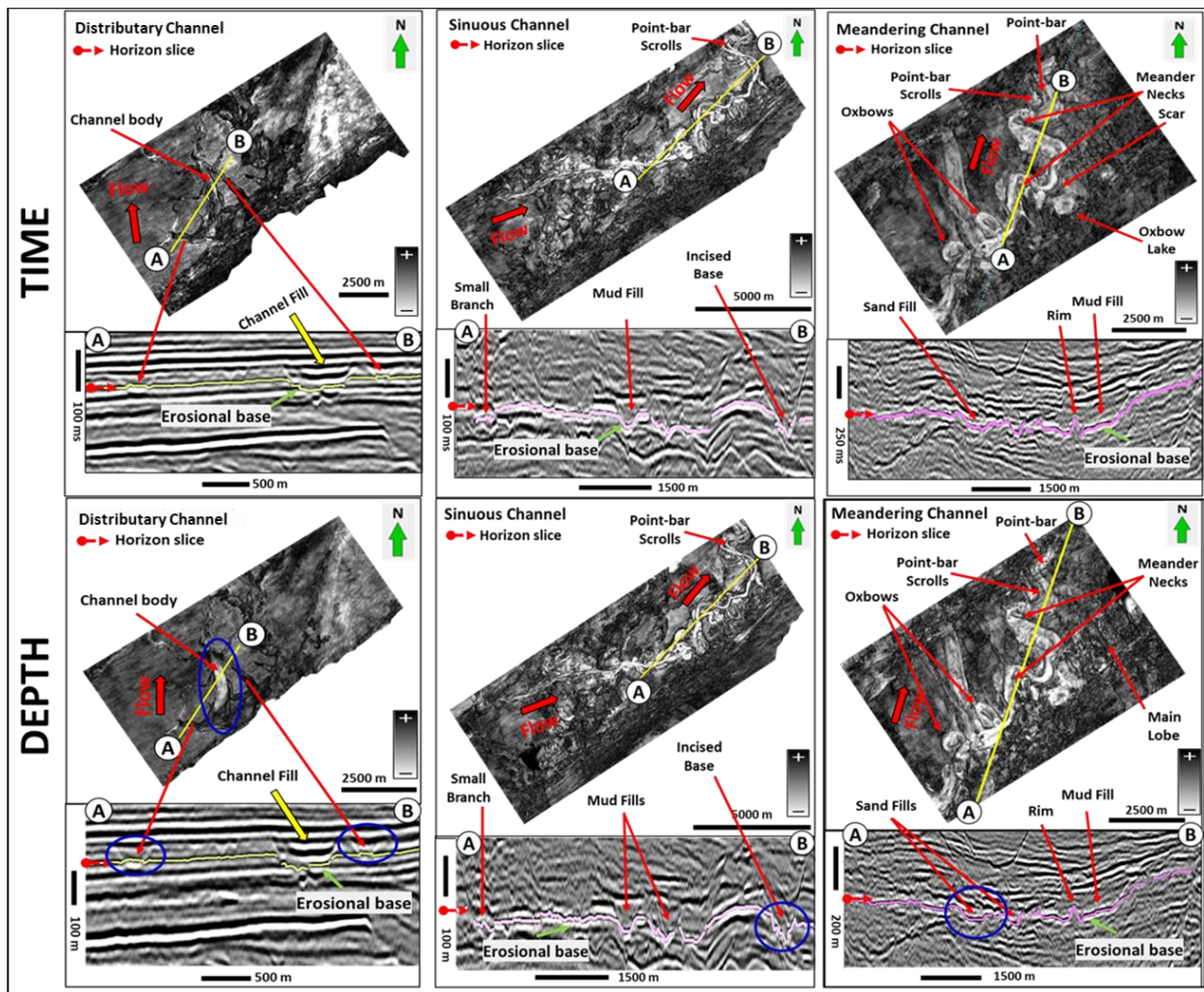


Figure 2. 7: Interpretational comparison of channels over the time and depth domains using extracted horizon slices (D, S, and M) from RMS amplitude volumes.

After the interpretation phase was completed, dip and azimuth, the Sobel Filter similarity, energy ratio similarity, the most positive and the most negative curvature, envelope, instantaneous phase, and the spectral decomposition attributes were chosen to be evaluated and analyzed in the time and depth domain. For these, the channels in the Giant Foresets Formations, faults 1, 2, 3, and 4 in the Turi Fault Zone were chosen as focused areas of interest to perform the detailed analysis on.

Results

The interpretations in two domains revealed that fault dips increased significantly (Fig. 2. 6) in the depth-migrated data. A remarkable change in the azimuth angles of the faults was not observed. It is because the depth migration method does not rotate the fault plane. When compared to the time migrated dataset, the channels in depth domain had narrower edges and steeper dips (Fig. 2. 7). This is the result from higher lateral resolution and relatively more accurate geologic positioning of the elements in the depth algorithm. The most significant difference is the main body appearance of the distributary channels in the two domains. In the depth data, the distributary channel and its distributary branches can be more easily determined than in the time domain. In the meandering channel, on the other hand, the data clearly showed the main channel lobe which is difficult to see in the time domain.

Seismic Attribute Analysis

In this section, I used geometrical, physical, and spectral seismic attributes to make a more detailed analysis of the variations observed in the conventional seismic interpretations. Table 2. 3 consists of detailed explanations about the seismic attributes I used in this investigation.

Table 2. 3: Seismic attributes used in study (summarized from Roden, 2015; Taner, 1994).

CATEGORY	TYPE	INTERPRETIVE USE
Geometrical Attributes	Dip, Coherence/Similarity, Variance, Curvature	Faults, Fractures, Continuity, Edge Detection
Physical Attributes	Envelope, Instantaneous Phase, Instantaneous Frequency, Sweetness	Lithology Contrasts, Bedding Continuity, Stratigraphic Variations
Spectral Decomposition	Short-time Fourier Transform (STFT)	Layer Thickness, Stratigraphic Variations
Multispectral Coherence	Spectral components with coherence	Layer Thickness, Stratigraphic Variations

Geometrical Attributes

Dip and Azimuth

Rijks and Jaufred (1991) presented a convenient way to compute dip magnitude and dip azimuth parameters in fault delineation. The method is based on a simple principle that is placing a plane through the adjacent points and then, sending the computed dip magnitude values (in degrees or radians unit) to the central data point in accordance with a local reference point. The azimuth magnitude is a measure of the deviation angles for these points from the North direction. In this section, the dip3d program was applied to understand how dip and azimuth angles vary and the possible reasons. Figure 2. 8 shows the result of our experiments.

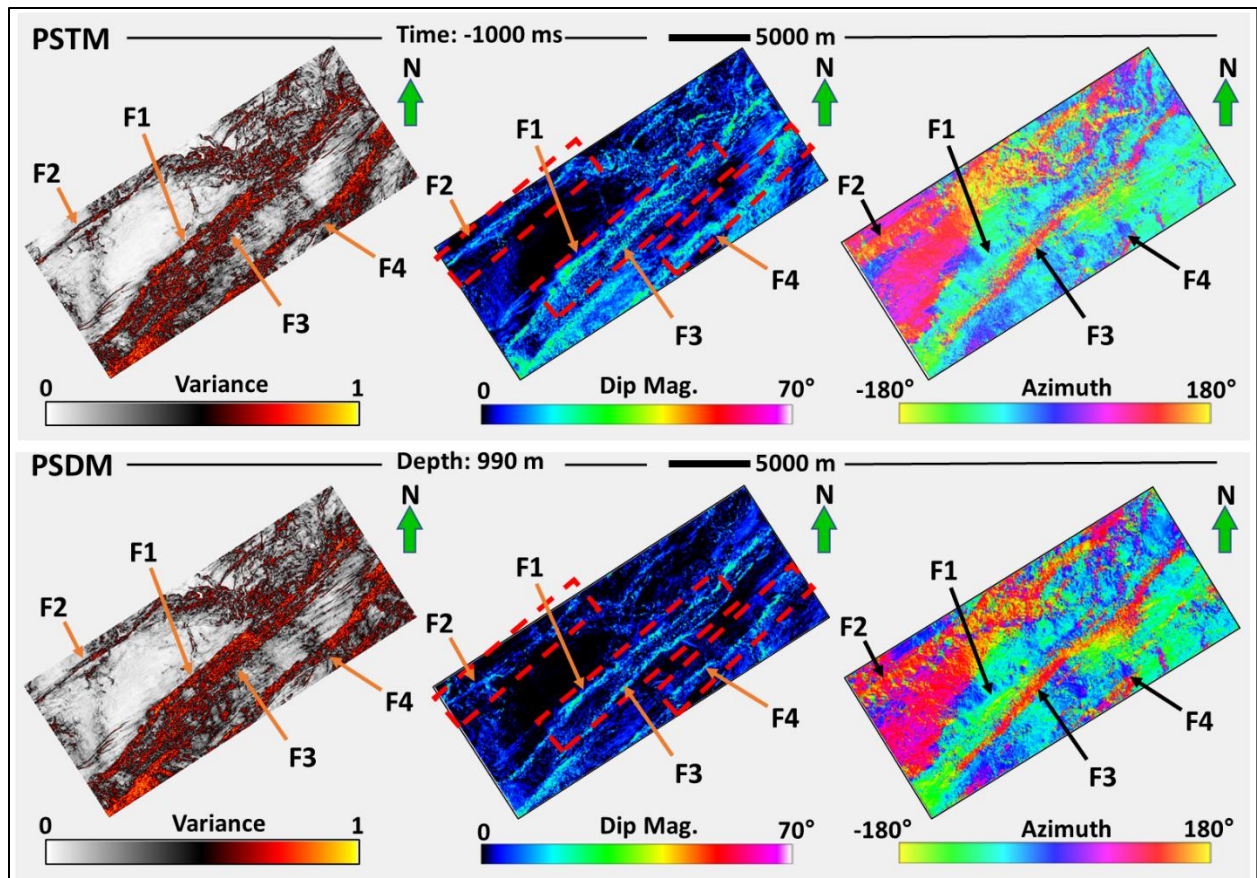


Figure 2. 8: The time slices at the top show variance, dip, and azimuth in the time domain, respectively, from left to right. The depth slices at the bottom show the equivalents of the top ones in the depth domain. Orange and black arrows show faults. The red dashed rectangles depict dip changes in both domains.

The comparisons (Fig. 2. 8) proved that the dip degrees have a significant increase in the depth domain, whereas azimuth degrees did not exhibit meaningful variations. This is because the depth migrated algorithm does not affect the fault plane direction relative to the north. The reason causing variations in fault dips is the depth migration algorithm itself. As I previously mentioned, depth migration requires an updated velocity model and iterative topographic corrections. Additionally,

it accounts for ray bending at the interfaces and uses interval velocities rather than average. The approach that assumes velocities are changing both vertically and horizontally with increasing depth, causes to decrease in the travelttime of the rays traveling between the receiver and the point at the subsurface. Thus, faults look steeper in the depth-migrated data. The highest difference was observed in the dip comparison of Fault 1 which is 20° in the time domain whereas 60° in the depth domain (Appendix D and E). Dip and azimuth variations were also visualized in a 3D display for each fault (see Appendix D and E).

Coherence

Chopra and Marfurt (2007) defined coherence as a measure of similarity between waveforms or traces. It is crucial to highlight the geometrical parameters of structural and stratigraphic features in 3D seismic interpretation. Working with low-quality data requires extra effort to identify their existence, shapes, direction, edges, length, discontinuity, and proper interpretation. To address this issue, Bahorich and Farmer (1995) proposed a method based on computing coherence coefficients from seismic amplitudes on neighboring traces using a cross-correlation technique. This method clearly depicted faults, buried deltas and river channels.

Luo et al. (1996) generalized the Sobel Filter which is an immensely popular tool used for photo enhancement and embedded in the most digital cameras on the market and introduced a useful method for edge detection. The inline and crossline derivatives are normalized by the energy in this method which is applied to seismic data to highlight faults, channel edges and fractures.

After the three-trace cross-correlation method, introduced by Bahorich and Farmer in 1995, which is sensitive to noise, Marfurt et al. (1998) generalized this method using the arbitrary number of input traces. This method is called multi-trace semblance-based coherence. However, semblance-based coherence is sensitive to changes not only in waveform but also to the lateral changes of seismic amplitudes. To overcome this issue, they developed the eigenstructure-based coherence algorithm which is computed from the eigenvalues of the covariance matrix. Then, Chopra and Marfurt (2007) introduced another method, energy ratio coherence (or energy ratio similarity), which is the ratio between coherence and the sum of the energy of traces used in the analysis window.

In the coherence attributes shown in Figures 2. 9 and 2. 10 (Sobel Filter and energy ratio similarity respectively) that are measuring the waveform or trace semblance, the trace models reflecting our expectations from the tests were created. In Figures 2. 9 and 2. 10, a and d show these trace models for the time and depth domain, respectively. According to the trace models, depth migrated data that have higher lateral resolution, accuracy, and brighter reflections should exhibit relatively high coherence values compared to the time domain that has higher vertical resolution. In another saying, channel edges should be highlighted better in the time domain. As expected, channel edges causing discontinuities in seismic data were better highlighted due to a relatively lower trace similarity characteristic of time-migrated data as well as its superiority on the vertical resolution. Similar to the situation with the Sobel filter, the observations in the energy ratio similarity attribute indicate that the time domain data was superior in highlighting the channel edges and provided a better visualization.

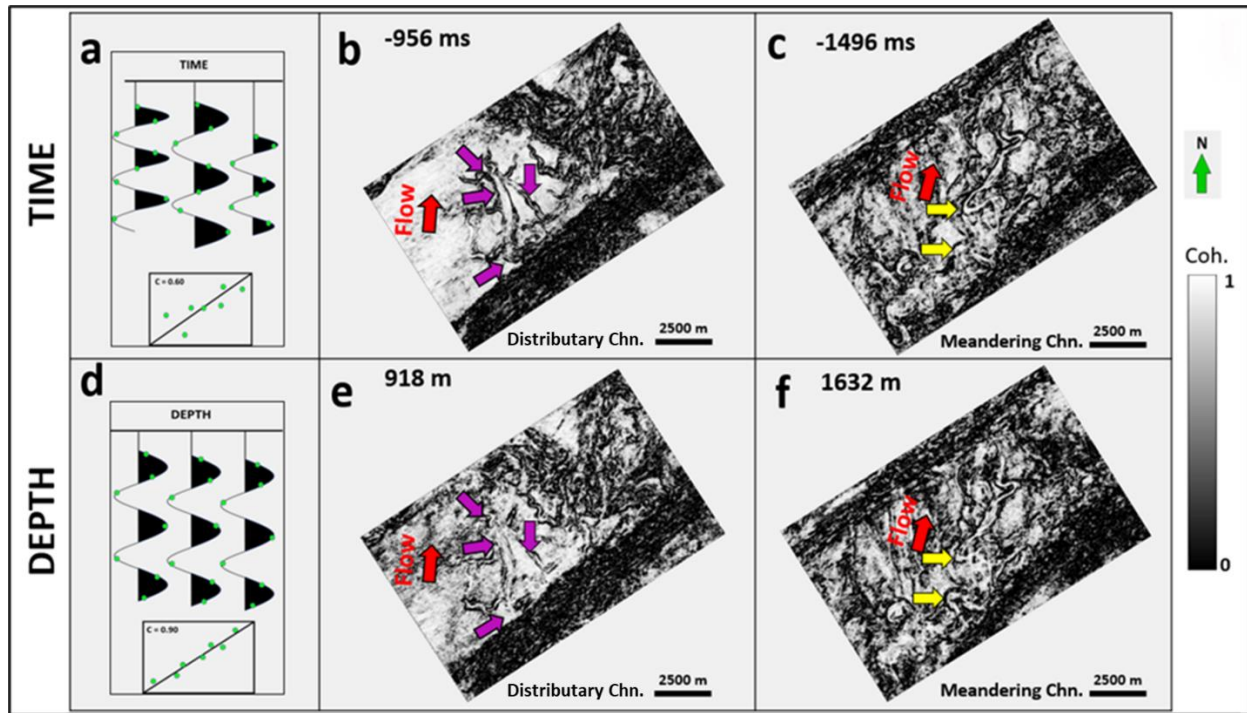


Figure 2. 9: The Sobel Filter attribute comparison with time and depth slices. a) Trace semblance model for time-domain and d) for the depth domain. The top two (b, c) represents the time domain and the bottom group (e, f) corresponds to the depth domain equivalents. The same-colored arrows are used to highlight variations in the same part of the stratigraphic events in both domains.

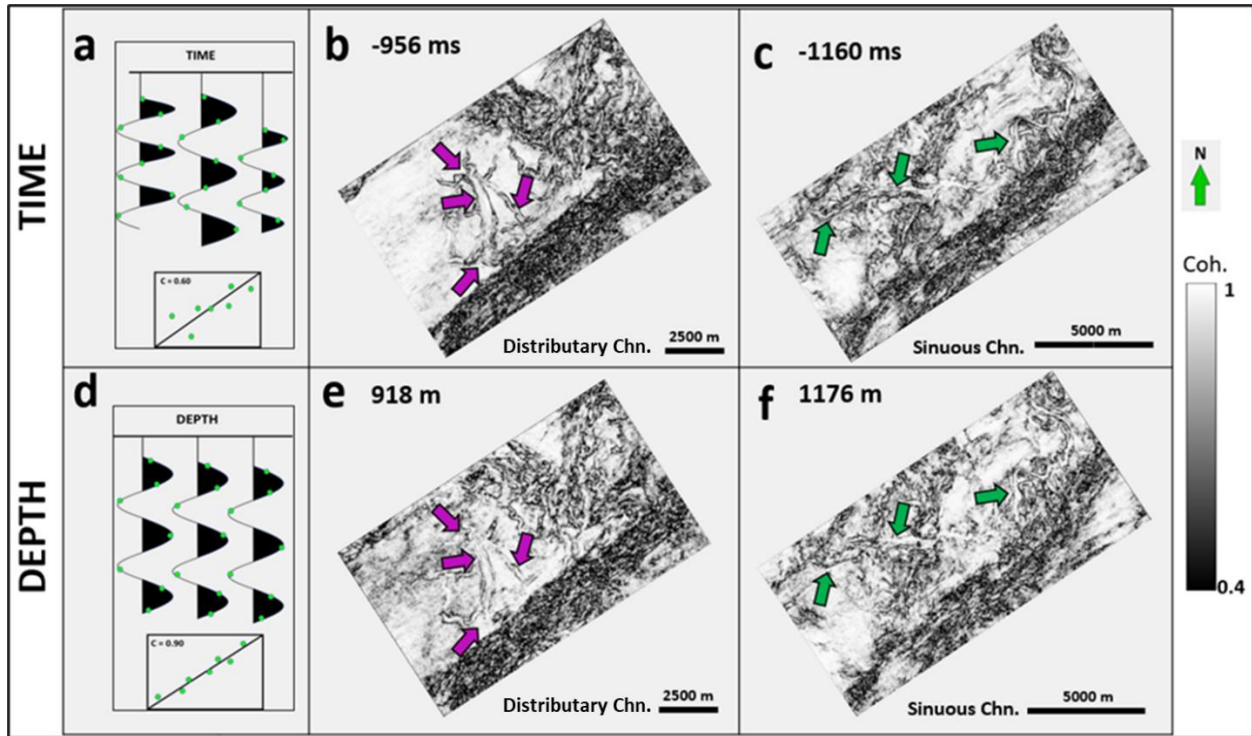


Figure 2. 10: The energy ratio similarity attribute comparison with time and depth slices. a) Trace semblance model for time domain and d) for the depth domain. The top three (b, c) represents the time domain and the bottom group (e, f) corresponds to the depth domain. The same-colored arrows are used to highlight variations in the same channels in both domains.

Curvature

Curvature is a measure of how the curve is bent relative to a given particular point, or how much it deviates from a tangent straight line from that point, and it is a two-dimensional property of a curve (Roberts, 2001). The curvature attribute has been used to delineate faults and fractures on seismic sections. Lisle (1994) introduced an extremely useful method to understand the folding structures and characteristics of the open fractures and showed the application of Gaussian Curvature (K) on a given structure or a part of a structure. In case of folding, this method shows the change of curvature values at a given point as a product of the two principal curvatures, k_1 and

k_2 , measured along two perpendicular curves through that point. Roberts (2001) calculated the most positive and most negative curvatures by setting the inline and crossline dip coefficients to zero. Roberts (2001) says that there is an inverse relationship between the radius of curvature value and the bending of the curve. It means the smaller radius of curvature causes larger curvature. The models were created for both domains by using his theory (Fig. 2. 11a and b) and co-rendered the most positive and the most negative curvature attributes to analyze normal faults (Fig. 2. 11c and d).

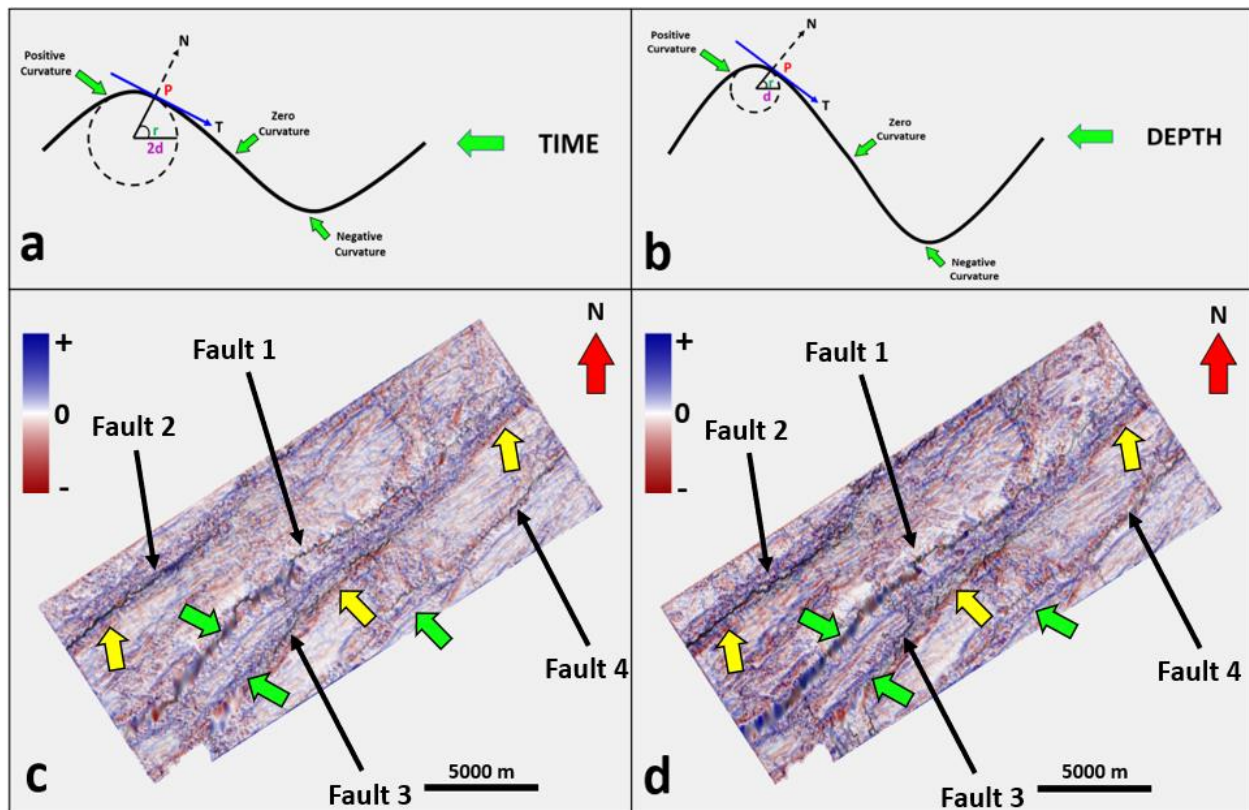


Figure 2. 11: The comparison of co-rendered the most positive and the most negative curvature attributes on the Matemateonga horizon. a) the curvature model for the time domain, b) the curvature model for the depth domain, c) the extracted horizon in the time domain, d) the extracted horizon in the depth domain. The black arrows show the faults, green arrows point to the most

positive curvature variations, and yellow arrows shows the most negative curvature variations between the time and depth-migrated datasets. Assuming that the dip angles of the faults are higher in the depth domain, the radius of the curvature should be smaller compared to the time domain. Therefore, larger curvature was observed in the depth-migrated data.

After structural analysis, the curvature model is assessed on the distributary channel by adding the expected architectural model to check variations in a stratigraphic feature (Fig. 2 12).

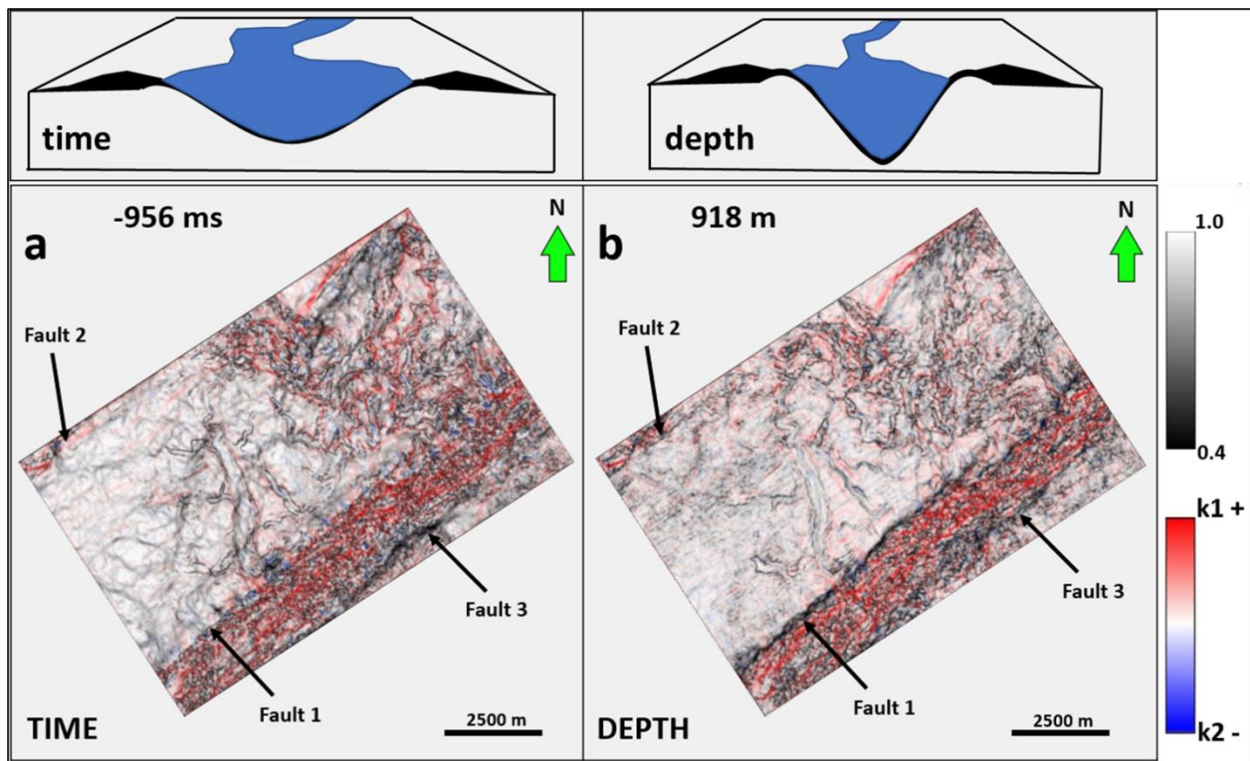


Figure 2. 12: The comparison of co-rendered the most positive, the most negative curvature, and the energy ratio similarity attributes with time and depth slices. The top two boxes show the expected channel geometry in both domains (Figure 2. 12a shows the time domain and Figure 2. 12b represents the depth domain). The black arrows show the faults.

Assuming that the channel edges are steeper, and the bodies are narrower in the depth domain, the radius of the curvature should be smaller compared to the time domain. Larger curvature in the depth-migrated data. In addition, this co-rendered analysis provided an incredibly detailed visualization for the distributary channel in the time-migrated data. It perfectly delineates almost all branches of the channel that I did not observe in the Sobel Filter and energy ratio similarity attributes. Note that faults are imaged better in the depth-migrated data (Fig. 2. 12).

Physical Attributes

Taner et al. (1979) introduced the complex trace analysis concept which allows us to examine the local variations on a given seismic signal. This method accepts a seismic trace as two parts: real part and conjugate or imaginary part. Calculation of the complex trace made it possible to define the instantaneous amplitude (envelope), phase and frequency component of the signal. They showed that the real part of the seismic trace can be expressed with a time-dependent amplitude and phase. One of the commonly used attributes, the instantaneous frequency, represents the rate of change of the time-dependent phase. Then, the imaginary part was created by using the Hilbert transform of the real trace. Radovich and Oliveros (1998) described another useful attribute called “sweetness” for the stratigraphic interpretation. It is derived by dividing reflection strength (envelope) by the square root of instantaneous frequency. All these attributes are especially useful to highlight the major lithological changes including bed thickness, sequence boundaries, bright spots, unconformities, and acoustic impedance contrasts.

Yilmaz (2001) showed that amplitudes were exhibiting relatively higher values in depth migration by using a salt diapir model. A simple model was created to show amplitude differences between the time and depth domains and our expectations upon it (Fig. 2. 13a and d). Envelope and instantaneous phase were applied to understand the variations of the channel interpretation over the time and depth domains. Figures 2. 13 and 2. 14 show the results of envelope and phase attribute analyses, respectively.

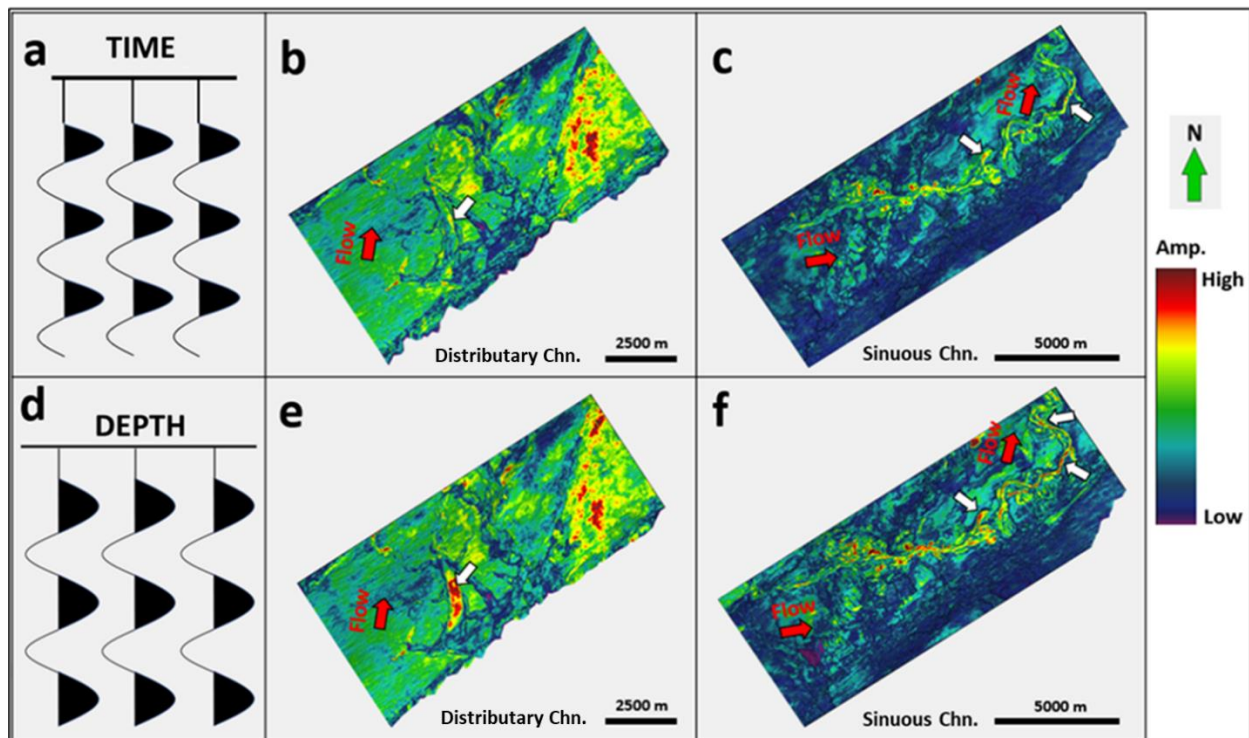


Figure 2. 13: Comparison of envelope attribute application using horizons slices D and S in both domains. a) the trace model for the time domain, d) the trace model for the depth domain. Channels shown in b and c are in the time domain while e and f in the depth domain. Depth domain data exhibit relatively brighter reflections (white arrows) due to the tuning phenomenon associated with the thin beds occurring when the bed thickness is one-quarter of a wavelength ($\lambda/4$).

The dominant frequency (f_d) in the area marked by the white arrow in Figure 2. 13e is 32 Hz and the interval velocity (V_{int}) is 2370 m/s. The tuning thickness, Z_t , can be calculated by $V_{int} / (4 \times f_d)$ formula. From this equation, Z_t is 18.52 m. Then, λ is calculated by V_{int} / f_d formula and it is 74.06 m. The calculations show that Z_t is approximately one-quarter of the wavelength which means a constructive interference creating brighter reflections in the depth migrated data.

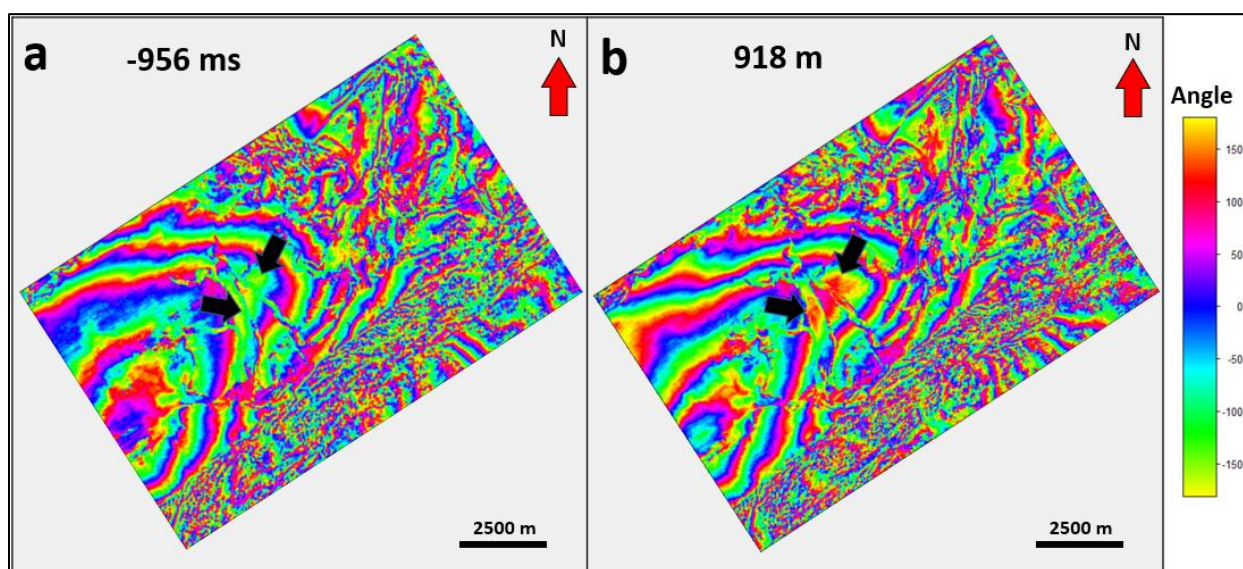


Figure 2. 14: Instantaneous phase comparison between the time and depth data with time and depth slices. The black arrows indicate changes in phase. Note the different phase in channel edges and faults between Figure 14a and b.

The results of the instantaneous phase attribute indicated phase contrasts in the channel edges and the faults in the depth domain (Fig. 2. 14b, black arrows). This is because dipping events and discontinuities create phase shifts in the seismic traces due to the side lobes interfering with each other. The instantaneous frequency test demonstrated frequency variations between the two

domains. Except for the distributary channel body, other frequency variations are caused by the frequency range difference (see Appendix – I). Sweetness attribute results also showed almost the same amplitude changes at the same part of the distributary channel (see Appendix – J) because it is derived by dividing reflection strength (envelope) by the square root of instantaneous frequency. It means that any changes in amplitude or frequency will create variations in the results.

Spectral Decomposition

Spectral decomposition (also known as time-frequency decomposition) is a widely used seismic attribute to support the seismic interpretation by improving thin-bed resolution and allowing the analysis of temporal bed thickness changes. Using spectral decomposition attribute, interpreters can analyze the structure in a wide frequency band. It can be performed in time data with units of Hz (cycles/second) or in depth with units of wavenumber (cycles/km). In the mid-1990s, Greg Partyka (1999) recognized that the lateral changes in frequency component were sourced by the variations in bed thickness and lithology. He created a short analysis window and showed a quantitative assessment by analyzing the amplitude spectrum of varying frequencies. This method is also known as short window discrete Fourier transform (SWDFT) and well-known as the spectral decomposition (Partyka et al., 1999). Sinha et al. (2005) introduced a novel approach to overcome window limitation by creating the continuous wavelet transform (CWT) technique which does not require a preselecting window length.

Small seismic cubes were created to cover the studied channels. Then, the frequency-amplitude spectrum was checked for each cube to determine the low, mid, and high frequencies that will be used while creating spectral decomposition cubes. Based on these frequency values, generalized

spectral decomposition (GSD) is performed, which simply a conventional use of Short-time Fourier Transform (STFT) algorithm. Next, images are blended using RGB (red for low, green for peak or dominant and blue for high frequencies) mixer to analyze the selected frequencies and their variations in the stratigraphic elements in time slices. Although it is easy to check the frequency spectrums of the seismic data by displaying the spatial spectrum in the time domain, software packages do not commonly contain a tool to display the wavenumber spectrum of depth domain data. To overcome this, a method introduced by Veenhof (2016) is followed. This method simply shows how to convert wavenumbers into frequencies. Figures 2. 15 and 2. 16 indicate the time and depth slices respectively from seismic amplitude volume at the top and combining three spectral frequencies over channels at the bottom for both domains.

In the time data, three frequency ranges for the distributary channel are: 20 Hz (the lowest frequency range) in red color, 38 Hz (the dominant frequency) in green color and 68 Hz (the highest frequency range) in blue color. For the sinuous channel, frequency ranges: 23 Hz (the lowest frequency range) in red color, 42 Hz (the dominant frequency) in green color and 61 Hz (the highest frequency range) in blue color. Finally, the frequency range for the meandering channel: 20 Hz (the lowest frequency range) in red color, 40 Hz (the dominant frequency) in green color and 60 Hz (the highest frequency range) in blue color. The amplitude-frequency spectrum is presented in Appendix – K.

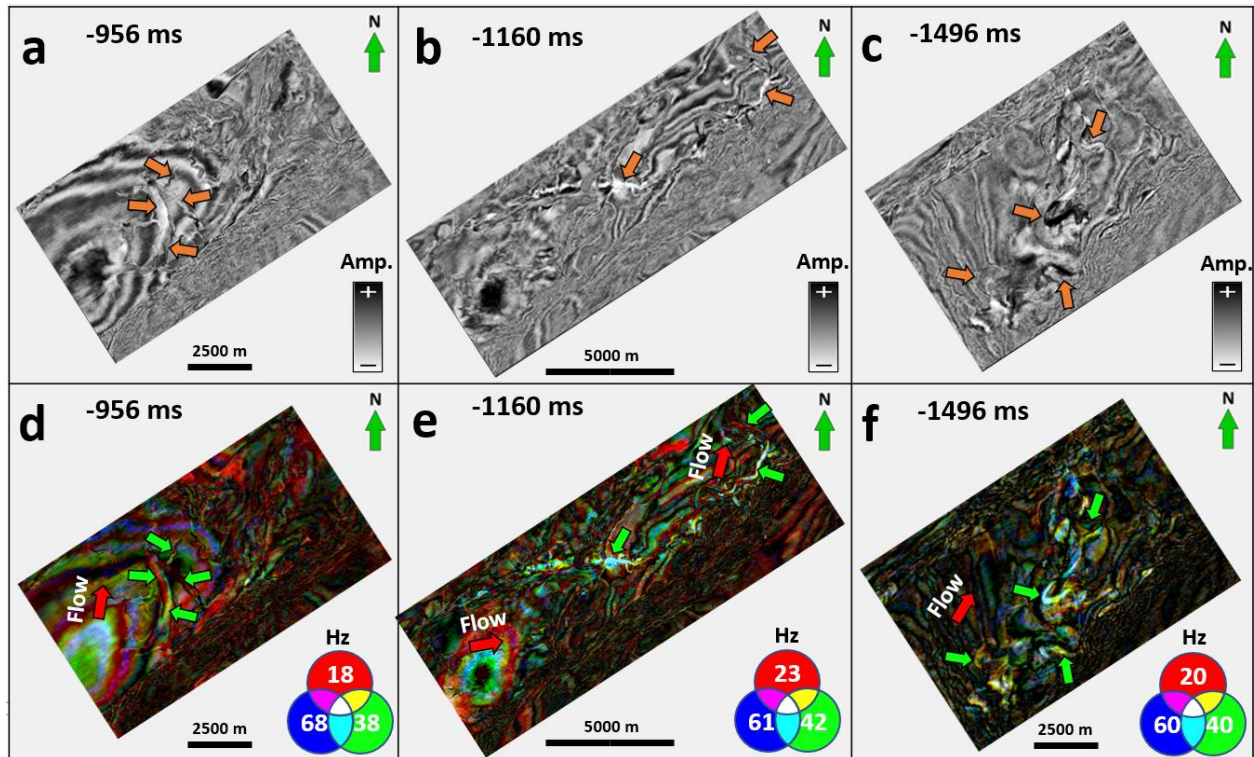


Figure 2. 15: Time slices with seismic amplitude (a-distributary channel, b-sinuous channel, c-meandering channel) and RGB spectral-decomposition blends (d, e, f). Orange arrows represent the prominent amplitude changes in a, b, and c, and the green arrows indicate corresponding frequencies for the same areas on the spectral decomposition RGB blended time slices for each channel. It is seen that bed thickness variations are clearly highlighted in the time migration data.

For the depth seismic data, three frequency ranges for the distributary channel are: 26 Hz (the lowest frequency range) in red color, 32 Hz (the dominant frequency) in green color and 38 Hz (the highest frequency range) in blue color. For the sinuous channel, frequency ranges: 22 Hz (the lowest frequency range) in red color, 28 Hz (the dominant frequency) in green color and 34 Hz (the highest frequency range) in blue color. Finally, the frequency range for the meandering channel: 20 Hz (the lowest frequency range) in red color, 25 Hz (the dominant frequency) in green

color and 30 Hz (the highest frequency range) in blue color. The amplitude-frequency spectrum was presented in Appendix – L.

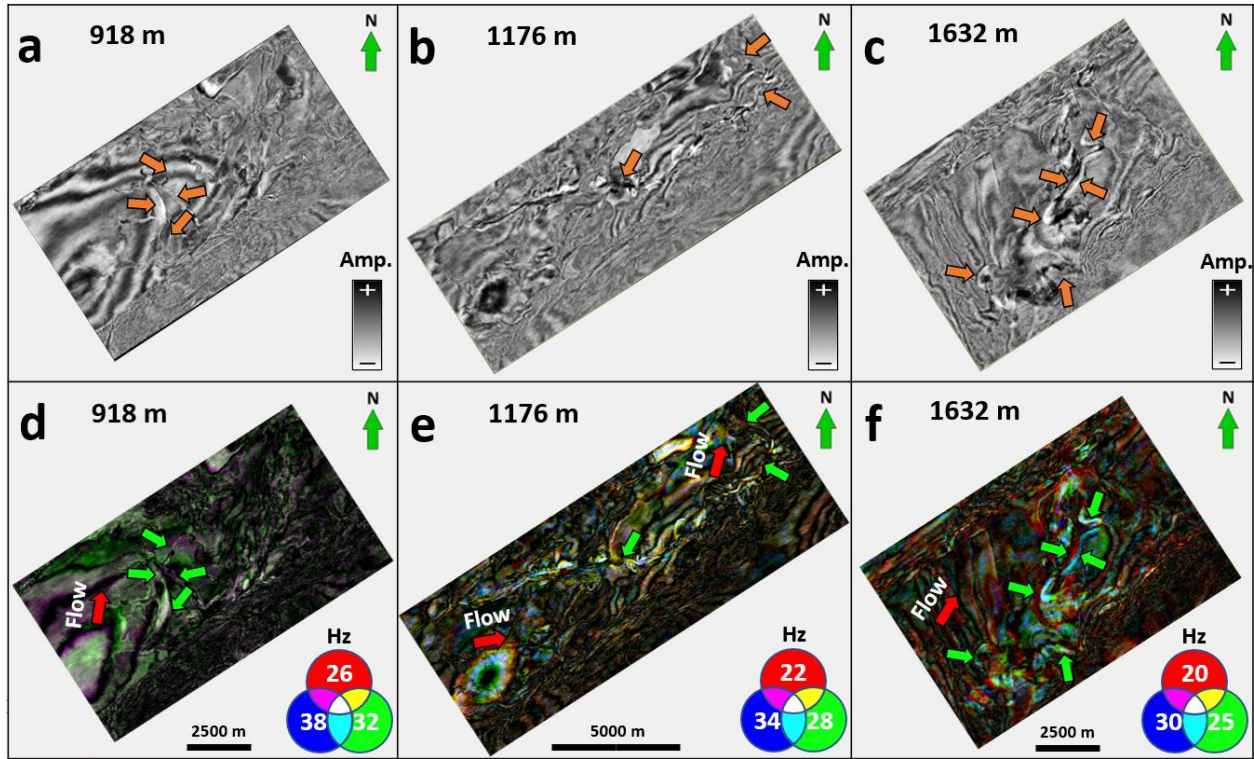


Figure 2. 16: Depth slices with seismic amplitude (a-distributary channel, b-sinuuous channel, c-meandering channel) and RGB spectral-decomposition blends (d, e, f). Orange arrows represent the prominent amplitude changes in a, b, and c, and the green arrows indicate corresponding frequencies for the same areas on the spectral decomposition RGB blended time slices for each channel. The bed thickness variations are better highlighted in the depth migration data.

In spectral decomposition results shown in Figures 2. 15 and 2. 16, channel parts tuned at a lower frequency (red color) are interpreted as coarse-grained sediments (possibly sandstones), whereas those tuned at an intermediate frequency (green color) represent the medium-grained sediments (possibly mudstones). The areas represented by the high frequency (blue color) correspond to the

fine-grained sediment deposition (possibly siltstones). Channel parts showing white color contain all frequencies while the dark parts do not contain any of the tuned values. The color differences are caused by different frequency ranges in both domains. In general, the results of spectral decomposition attribute test did not present significant variations which may lead to misinterpretation of the lithology inside and surrounding the channels between the time and depth domains. Multispectral coherence attribute was performed to see how frequencies are varying in the channel edges by using the same low-mid- and high frequencies (see the filter bank displays Appendix – M). The energy ratio similarity attribute was used as a coherence attribute (Appendix – N). The results indicate that there are frequency variations between the time and depth domains due to the frequency range difference.

Summary

As demonstrated with the various seismic attribute analyses, it is possible to quantify the existing interpretational differences, depending on whether the attribute is applied in the time or depth domain. These interpretational variations can range from small in scale (steeper channel walls and deeper channel beds, higher bending on fault planes) to larger (sharp increase in fault dips, different amplitudes within the channel bodies, and frequency differences both inside and around the channels). Based on the results of attribute-assisted qualitative and quantitative analyses, it can be concluded that the variations observed between the time and depth migration methods might affect the drilling plans, reservoir characterization, paleochannel studies, and lithologic classification in the targeted area. The results of the seismic analyses were discussed in detail in the discussion section.

Discussions

The time-migrated seismic data has inadequacies on imaging if the subsurface geology has strong lateral velocity variations and a geometrically complex structure. These disadvantages are mostly caused by the method used in the time migration. To solve these problems, depth migration, which provides high lateral resolution and removes pitfalls that come from the time data, is applied to the seismic data. However, depth migration also contains its own downsides that affect seismic interpretation. This study demonstrates these variations using a variety of seismic attributes to help interpreters for avoiding misinterpretations. The findings presented in the study prove that there are significant geometrical and physical differences to be taken into consideration during the seismic interpretation between time- and depth-migrated datasets.

The findings show high consistency with the models initially created for each attribute and match with the previous studies which identify the fundamental differences between the PSTM and PSDM datasets. Furthermore, the results not only prove the existence of these variations but also subject the inputs to a variety of seismic attribute tests to increase the interpretation quality and analyze the variations in detail.

The geometrical differences observed on the faults may affect the decision-making processes in determining the drilling location. Even though it is known that depth conversion of the time data still cannot provide the real seismic velocities about the subsurface, considering that it is obtained by many iterative processes along with geomorphologic corrections, depth-migrated data looks more dependable to decide. I do not aim to draw attention only to the positioning of the geological events but observed physical variations such as frequencies, phase, and amplitude might cause

mislead interpreters about the oil and gas presence in the exploration studies. Given the large budgets allotted to these studies, the significance of our findings grows even more.

The generalizability of the results is limited by one specific migration algorithm used to create both time and depth datasets, the Kirchhoff Migration. In addition, due to the lack of well data in the 3D seismic area, our lithological analysis for the channels formed in the Giant Foresets Formation is limited. However, despite all these limitations, this research proved the reliability of the findings by using seismic attributes. Another limitation of our study is that analyzed channels are located in the shallow and the youngest formation of the datasets.

Dip attribute analyses (Table 2. 4) demonstrated that fault dips increased dramatically in the depth-migrated data. The reason causing variations in fault dips is the algorithmic difference between the two methods. The time migration algorithm assumes a constant velocity gradient and does not account for the ray bending at interfaces. Considering that velocities increase with depth, the dips of the faults tend to be lower as depth increases. The depth migration algorithm, on the other hand, requires an update for the velocity model created in the time domain, then, takes this updated velocity model and assumes that rays are bending at interfaces. If there are robust lateral velocity changes, it means velocities are changing both vertically and horizontally. While the vertical velocity increase pushes the faults to become more curve in the deeper parts, the lateral changes force them to become steeper. It is because lateral velocity increase shortens the travel time of the rays between the receiver and the point.

Sobel Filter and energy ratio similarity analyses (Table 2. 4) showed that faults were clearly delineated in the time-migrated data than depth-migrated. The main reason is the existence of amplitude differences between the two domains. Both attribute algorithms create maps by taking the semblance of amplitudes along the adjacent traces. Considering that reflections are more continuous and relatively brighter in the depth-migrated data and since the coherence algorithm is more sensitive to discontinuities, in the time domain, faults were detected better than the depth domain. The channel edges creating discontinuities were also delineated better in the time domain because of the same reason.

Curvature attribute analyses (Table 2. 4) showed larger positive and negative values in depth-migrated data. Based on the model created, the attribute algorithm takes higher values when the radius of the peak or trough is smaller. I know that events exhibit steeper shapes in depth-migrated data. These conditions create a smaller radius and increase the curvature of faults and the same situations apply to the channel walls as well, thus, I observed larger curvatures in the channel edges and beds.

Table 2. 4 – The summary of the results for each seismic attribute analysis evaluated on geologic events. Green boxes represent the geometric variations, blue boxes indicate physical variations and yellow boxes show spectral variations.

Seismic Attribute	PSTM DATA							PSDM DATA						
	FAULTS				CHANNELS			FAULTS				CHANNELS		
	F1	F2	F3	F4	DIS	SIN	MEA	F1	F2	F3	F4	DIS	SIN	MEA
Dip Mag. Max. (°)	C - 16	C - 35	C - 52	C - 56	-	-	-	S - 62	S - 56	S - 62	S - 66	-	-	-
Dip Azi. Max. (°)	310	150	135	310	-	-	-	310	150	135	310	-	-	-
Variance (0-1)	L	L	L	L	-	-	-	H	H	H	H	-	-	-
Sobel Filt. (0-1)	H	H	H	H	W	W	W	L	L	L	L	N	N	N
Energy Rat. Sim. (0-1)	H	H	H	H	W	W	W	L	L	L	L	N	N	N
Curvature (+) – (-)	L - L	L - L	L - L	L - L	SBE	SBE	SBE	H - H	H - H	H - H	H - H	HBE	HBE	HBE
Envelope (Amp)	-	-	-	-	L	L	NC	-	-	-	-	H	H	NC
Inst. Phase (°)	-	-	-	-	-120	SC	SC	-	-	-	-	+120	SC	SC
Inst. Frequency D. (Hz)	-	-	-	-	38	42	40	-	-	-	-	32	28	25
Sweetness (Amp)	-	-	-	-	L	L	NC	-	-	-	-	H	H	NC
Multispect. Coh. D. (Hz)	-	-	-	-	40	42	38	-	-	-	-	25	28	32
Spect. Decomp. (Hz)	-	-	-	-	38	42	40	-	-	-	-	32	28	25

Explanations of the abbreviations			
■ Geometric	F1 → Fault 1	C → Curved	L – L → Low Positive and Low Negative Curvature
■ Physical	F2 → Fault 2	S → Steeper	H – H → High Positive and High Negative Curvature
■ Spectral	F3 → Fault 3	L → Low	SBE → Small Bending Edges (channel walls)
	F4 → Fault 4	H → High	HBE → High Bending Edges (channel walls)
	DIS → Distributed Channel	W → Wider	NC → No Changes
	SIN → Sinuous Channel	N → Narrower	SC → Small Changes
	MEA → Meandering Channel		

Envelope attribute tests (Table 2. 4) demonstrated relatively brighter spots inside the distributary channel in depth-migrated data compared to time because of the tuning phenomenon. The phase difference was observed in the distributary channel body, which might be interpreted as a lithologic variation (Table 2. 4). However, the reason is more likely the interference of the seismic trace lobes due to the dipping reflections. The co-rendered instantaneous frequency and the Sobel Filter attribute results (Table 2. 4) demonstrated that frequencies range from 30 to 50 Hz within the

distributary channel in the time domain whereas they range between 20-40 Hz in the depth domain (see Appendix Ia-d). Additionally, frequencies are around 40 Hz in the middle and the northeastern part of the sinuous channel (see Appendix Ib-e) while they range between 25-35 Hz in the depth domain. These variations might be caused by the natural frequency differences between the two domains (in depth domain, frequencies are relatively lower than the time domain). The infill sediment differences, or bed thickness variations might be alternative explanations for the frequency variations.

The sweetness attribute assesses (Table 2. 4) indicated that depth domain data exhibits relatively high amplitudes within the channel bodies depicted in Appendix Ja, b, d, and e. The observed variations support the previous envelope attribute test results and are caused by the same reasons. The spectral decomposition tests (Table 2. 4) did not indicate significant frequency variations in the channel beds or around except for the negligible ones. It is known that the depth domain has always lower frequencies, but they did not indicate high differences in RGB blended frequency analyses. Multispectral coherence attribute results (Table 2. 4) indicated that discontinuities (channel edges) have frequency variations just like observed in the instantaneous frequency attributes (Appendix N). However, since there are frequency range differences between the two domains, these variations cannot be interpreted as lithologic or geometric changes. The reason that causes variations is that the energy ratio similarity attribute values.

The PSTM data was converted to depth by creating a velocity model using the interval velocity data, then, it was compared with the PSDM data to understand how faults and horizons are changing geometrically (Fig. 2. 17). The results indicated that fault dips remained almost the same

between both datasets whereas horizons resembled the PSDM data (blue ellipses, Fig. 2. 17). Horizons got flatter in the new PSTM volume compared to Figure 2. 6. However, with depth-converted PSTM data, it is harder to distinguish interpretational variations.

The Sobel Filter similarity attribute was recalculated using depth-converted PSTM volume as an example, then, compared with the PSDM volume (Fig. 2. 18). The comparison in the left column represents the original PSTM and PSDM whereas the right column shows the depth-converted PSTM and PSDM comparison. It is clear that before depth conversion, there were a lot of geometrical variations between the two domains. Channel edges were better highlighted in the time domain due to the time migration method's advantage in catching the discontinuities that have relatively small dips. Another reason is that depth migration improves the continuity of the reflections and provides higher lateral resolution. After depth conversion, all geometric variations almost disappeared, and it is no longer possible to differentiate between two data sets (check the red arrows, Fig. 2. 18).

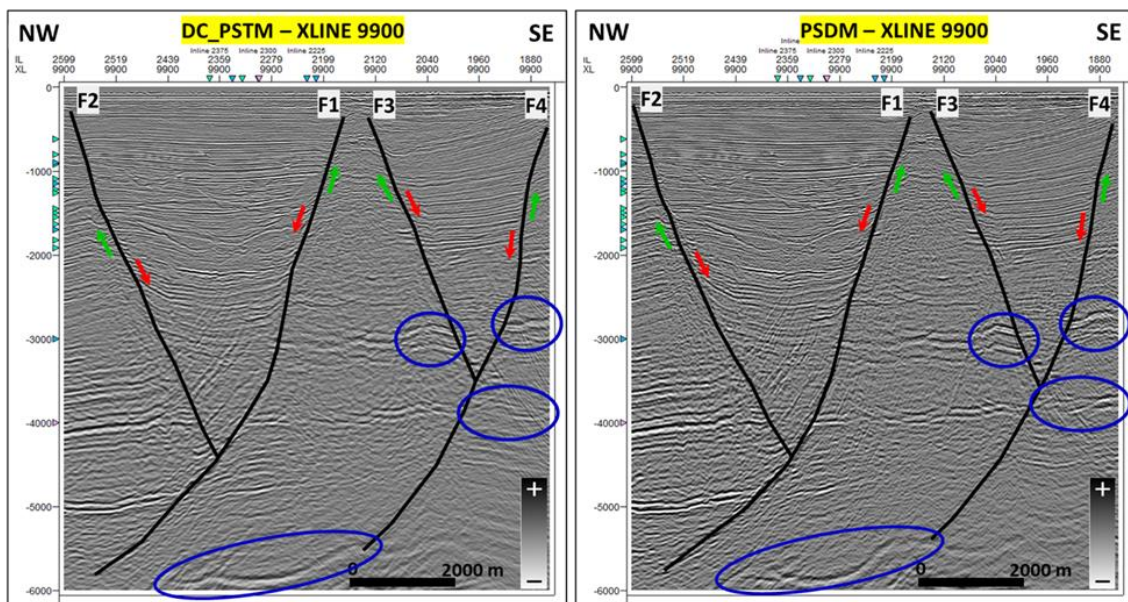


Figure 2. 17: Fault dip comparison between the depth-converted PSTM (left) and PSDM datasets. Blue ellipses indicate variations observed on horizons.

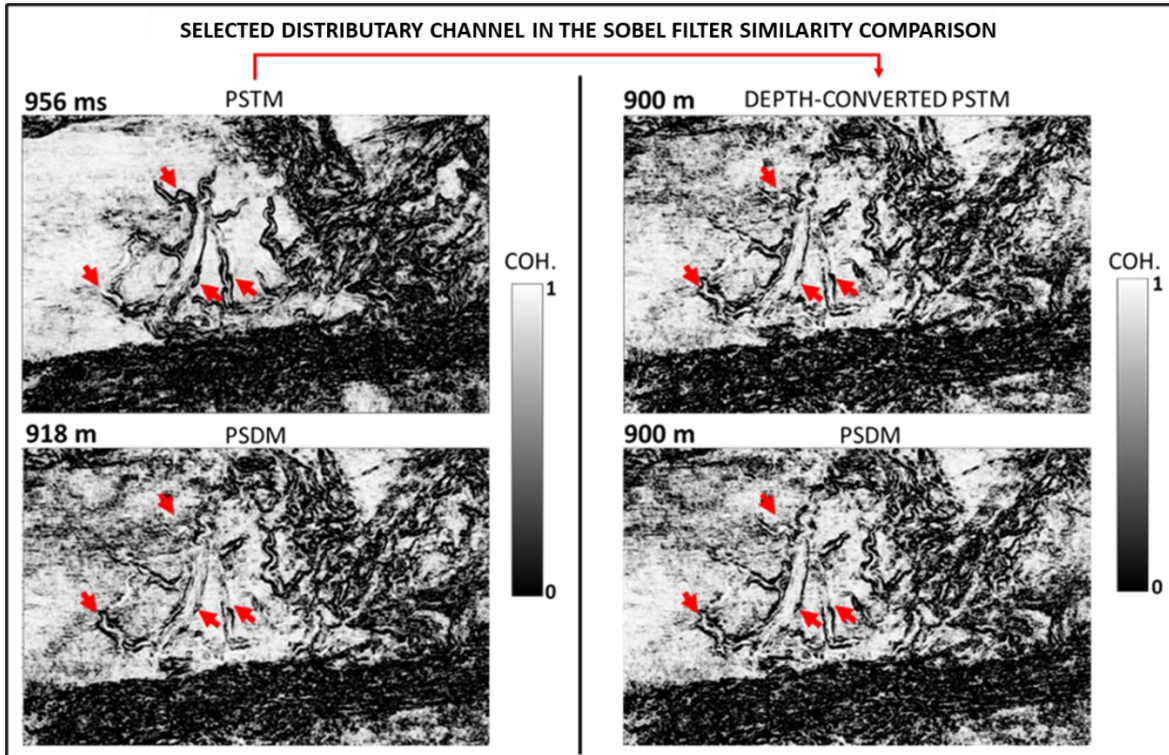


Figure 2. 18: The Sobel Filter similarity comparisons between the depth-converted PSTM and PSDM datasets. Red arrows indicate the geometric variations in the distributary channel.

Finally, it is strongly recommended that interpreters who work with depth-migrated data should be aware of significant differences presented in this study and make their interpretations by comparing both domains with a seismic attribute-assisted workflow before the final decision.

Conclusions

This research aimed to understand the interpretational variations and similarities between the pre-stack time- and depth-migrated datasets using seismic attribute-assisted methods. In accordance

with this purpose, I evaluated a wide range of geometrical, physical, and spectral attributes to analyze both structural and stratigraphic elements. Based on the qualitative and the quantitative analysis it can be concluded that there are significant differences in the imaging and interpretation of the same geologic events defined in both domains.

First of all, I thought about why depth migration is necessary. The literature scanning showed that the strong lateral velocity changes and complex geology need depth migration. The data set used in this study was obtained from an area with just such a geology and each used seismic attribute was selected in accordance with the feature desired to be analyzed. In the previous studies, I recognized what type of fundamental methodologic differences or similarities I should expect between the time and depth migration methods.

At the beginning, I expected that the dip and azimuth magnitudes of the faults should be higher in the depth-migrated data due to its superiority in the lateral resolution and its creation using a relatively more consistent velocity model. I also expected to see narrower channel bodies and steeper channel edges in the depth domain and the reflections should have been brighter in the depth domain. Thus, I designed simple hypothetical models for each attribute experiment. The results of the geometric attributes demonstrated that the dip magnitude of the faults is remarkably higher in the depth domain while azimuth angles stayed the same. This characteristic caused higher curvature values due to more bending. The channel architectures exhibited narrower characteristics with steeper edges in depth-migrated data. The result of the physical attribute tests indicated relatively brighter reflections and phase variations (in distributary channel bodies) but slightly different frequencies, especially in the channel bodies, which can be interpreted as lithologic

changes. In conclusion, our expectations very highly matched with the obtained results except for azimuth angles.

Based on these conclusions, it is recommended that seismic interpreters should take into consideration that depth conversion can cause interpretational variations, and thus, geologic events can be misinterpreted. In this study, only the Kirchhoff migration method has been considered. To better understand the implications of the results, future studies could address other types of migration algorithms to see the possibility of reducing interpretational variations between the time and depth domain.

Acknowledgments

The authors thank the Turkish Ministry of Education for funding A. Murat Alyaz to study at the University of Oklahoma. I would like to thank New Zealand Petroleum and Minerals for providing the datasets used in this study. I thank Schlumberger for the Petrel software and the University of Oklahoma for providing these licenses to the researchers. I also thank the AASPI consortium and its members. Special thanks to Dr. Kurt Marfurt and the AASPI group led by Dr. Heather Bedle for constructive discussions and recommendations. I also thank Dr. Gokay Bozkurt from TotalEnergies for his valuable contributions and feedback.

Data and material availability

The datasets used for this research are publicly available on the New Zealand Petroleum and Minerals website www.nzpam.govt.nz

References

Bahorich, M., and Farmer, S., 1995, 3-D seismic discontinuity for faults and stratigraphic features: The coherence cube: *The Leading Edge* 1053-1058.

Bradley, B. A., and Cubrinowski, M., 2011, Near-source Strong Ground Motions Observed in the 22 February 2011 Christchurch Earthquake: *Seismological Research Letters*, Vol. 82., No. 6.

Cameron, H. E., 2016, Evolution of a normal fault system, Northern Graben, Taranaki Basin, New Zealand: M.S. thesis, Victoria University of Wellington.

Chopra, S., and K. J. Marfurt, 2007, Seismic attributes for prospect identification and reservoir characterization: *SEG Geophysical Development Series*, 11.

Chopra, S., and Marfurt, K., 2007, Curvature attribute applications to 3D surface seismic data: *The Leading Edge* 2007.

Etgen, J. T., and Kumar, C., 2012, What really is the difference between the Time and Depth Migration? A tutorial: *SEG Las Vegas 2012 Annual Meeting*.

Etris, E. L., Crabtree, N. J., and Dewar, J., 2002, True Depth Conversion: More Than a Pretty Picture, *CSEG RECORDER*, Vol. 26, No. 09.

Gazdag, J., and Sguazzero, P., 1984, Migration of Seismic Data: *Proceeding of the IEEE*, Vol. 72, No. 10.

Goodway, B., Purdue, G., Looi, S. Y., Du, L., Rowland, M., 2016, Depth Imaging for Unconventional Reservoir Characterization: Canadian Plains Case Study, *GeoConvention 2016*, Calgary, Canada.

Grigorova, M., 2016, Comparison between prestack depth migration and direct depth conversion of time migrated section using tomography-based velocity model: 2nd International Scientific Conference GEOBALCANICA 2016.

Hansen, R. J., and Kamp, P. JJ., 2001, Evolution of the Giant Foresets Formation, northern Taranaki Basin, New Zealand: New Zealand Petroleum Conference Proceedings 24-27 February 2002.

Hill, S., and Rüger, A., 2019, Illustrated Seismic Processing, Course Notes Series No. 15.

Jain, R., 2012, Kirchhoff Pre-Stack Depth Migration: effective tool for depth imaging: 9th Biennial International Conference & Exposition on Petroleum Geophysics, Hyderabad 2012.

King, P. R., and Thrasher, G. P., 1996, Cretaceous-Cenozoic Geology and Petroleum Systems of the Taranaki Basin, New Zealand: Lower Hutt Institute of Geological & Nuclear Sciences Limited.

Knox, G. J., 1982, Taranaki Basin, structural style and tectonic setting, New Zealand: Journal of Geology and Geophysics, 25:2, 125-140.

Kumar, P. C., 2016, Application of geometric attributes for interpreting faults from seismic data: an example from Taranaki Basin, New Zealand, SEG International Exposition and 86th Annual Meeting, p. 2077-2081.

Li, S., Fomel, S., 2014, A robust approach to time-to-depth conversion and interval velocity estimation from time migration in the presence of lateral velocity variations: Geophysical Prospecting, 2015, 63, 315–337.

Lin, T., 2015, Attributes Assisted Seismic Interpretation in Pre-Stack Time versus Depth Migration Data: AAPG Annual Convention & Exhibition 2015, Denver, Colorado, May 31-June 3, 2015.

Lisle, R., 1994, Detection of Zones of Abnormal Strains in Structures Using Gaussian Curvature Analysis: AAPG Bulletin, V. 78, No. 12 (December 1994), P. 1811-1819.

Luo, Y., Higgs, W. G., Kowalik, W. S., 1996, Edge detection and stratigraphic analysis using 3D seismic data: Interpretation 2: Structural Case Histories.

Marfurt, K. J., Kirlin, R. L., Farmer, S. L., Bahorich, M. S., 1998, 3-D seismic attributes using a semblance-based coherency algorithm: Geophysics, Vol. 63, No. 4 (July-August 1998); P. 1150 – 1165, 21 Figs.

Partyka, G., Gridley, J., and Lopez, J., 1999, Interpretational applications of spectral decomposition in reservoir characterization: The Leading Edge, 18, P. 353-360.

Pilaar, W. F., and Wakefield, L., 1978, Structural and Stratigraphic Evolution of the Taranaki Basin, Offshore North Island, New Zealand: Appea Journal.

Radovich, B. J., and Oliveros, R. B., 1998, 3-D sequence interpretation of seismic instantaneous attributes from the Gorgon Field: The Leading Edge 1998.

Rijks, E. J. H., Jauffred, J. C. E. M., 1991, Attribute extraction: An important application in any detailed 3-D interpretation study: Seismic Interpretation 29.

Roberts, A., 2001, Curvature attributes and their application to 3-D interpreted horizons: First Break, 19, 85–99.

Roden, R., Smith, T., and Sacrey, D., 2015, Geologic pattern recognition from seismic attributes: Principal component analysis and self-organizing maps: Interpretation, Vol. 3, Issue 4.

Sinha, S., Routh, P. S., Castagna, J. P., 2005, Spectral decomposition of seismic data with continuous-wavelet transform: *Geophysics*, Vol. 70, No. 6 (November-December 2005); P. P19 – P25, 9 Figs.

Taner, M. T., Koehler, F., Sheriff, R. E., 1979, Complex seismic trace analysis: *Geophysics*, Vol. 44, No. 6 (June 1979); P. 1041-1063, 16 Figs., 1 Table.

Taner, M. T., Schuelke, J. S., O'Doherty, R., Baysal, E., 1994, *Seismic Attributes Revisited*: SEG Technical Program Expanded Abstracts 1994.

TCPL Resources Ltd., 1989, PR1495, Okoki-1 QC and well summary report.

Terrace Marine & OBC 2D Reprocessing for Greymouth Petroleum., 2011, PR4436, Petroleum Report Series.

Thrasher, G. P., 1992, Late Cretaceous Geology of Taranaki Basin, New Zealand: Ph.D. thesis, Victoria University of Wellington. Trincherro, E., 2000, The fault shadow problem as an interpretation pitfall: *The Leading Edge*, P. 132-136.

Veenhof, R., 2016, Tip/Trick: Spectral Decomposition with Petrel: EBN Symposium 'Echoes from Seismic...'

Veritas Geophysical Asia Pacific Pte. Ltd., 2007, PR3741 - Toro 3D Seismic Survey Final Survey Report: Ministry of Economic Development New Zealand.

Yilmaz, O., 2001, *Seismic Data Analysis: Processing, Inversion, and Interpretation of Seismic Data*: Society of Exploration Geophysicists, Tulsa, OK, 1028 p.

Young, J., Johnson, G., Klug, Stephen., Mathewson, J., 2009, The Case for Depth Imaging All 3D Data: Complex Thrust Belts to Low Relief Resource Plays, WesternGeco; Denver, CO.

CHAPTER 3: FUTURE WORK

In this thesis, after detailed literature scanning about the fundamental differences between the time- and depth-migrated seismic data, the datasets, which belong to the Toro 3D seismic survey (Fig. 1. 1), to which both migration algorithms were applied due to the geology (Fig. 1. 2) studied were used. To analyze how seismic interpretation can vary in both structural and stratigraphic events, four faults and three channels were focused on in the conventional interpretation. Next, a variety of seismic attributes (Fig. 1. 5) were performed to improve and extend the first analyses obtained from the standard seismic interpretation, and the results were evaluated by doing comprehensive comparisons and discussions over both domains. According to the results discussed in Chapter 2 in detail, there are significant geometrical (shape, length, deep, wide, and dip) and physical (amplitude, phase, frequency) variations affecting the interpretation of the events between the two domains. The reasons for these results are presented in the light of the conceptual models that were previously designed for the seismic attribute tests.

However, only four normal faults and just three different channel types were selected to perform interpretational variation analysis in this research and the cropped volume corresponds to a small part of the entire cube. In addition, the seismic attributes used for the analyses are specific to the selected structural and stratigraphic events. Considering that the seismic well-tie had to be performed by using borehole data that is approximately 700 m far from the closest seismic line, it is clear that it is rather difficult to generalize the lithological analysis results. Despite all these limitations, the conventional interpretation and seismic attribute test results clearly showed that seismic interpretations have undergone remarkable changes between the two domains (Table-4). There are many more faults in the other parts of the area and tens of channels at different buried

depths. On the other hand, geology is not composed of only faults and channels, but it also includes fractures, folds, shear zones, canyons, deltas, turbidites, mass transport complexes, and valleys as well. Some of these events were seen during the standard seismic interpretation phase but were not included in the attribute analyses. However, they can be used to expand the scope of this research in future processes.

In this research, all the analyses were performed in the prestack migrated seismic datasets. However, stacking is one of the three most important steps in data processing and migration can be applied post-stack migrated seismic datasets as well. Therefore, it can be analyzed how seismic interpretations vary after stacking between the two domains as another future work. The workflow used here does not have any conditioning steps such as filtering or spectral balancing. The main reason for this is that the possible differences (e.g., frequency) between the two datasets will disappear during filtering or spatial balancing. The same datasets can be compared after data conditioning steps are applied. The results can be more similar or more different depending on the frequency, velocity, and depth of the area of interest. On the other hand, seismic attribute diversity can be increased by adding ant tracking used for fault enhancing and gray-level-co-occurrence matrix attributes (GLCM) used to analyze the texture of the seismic data with four key statistical parameters: energy, entropy, contrast, and homogeneity.

As it was explained in the earlier chapters, areas that have strong lateral velocities need depth migration to increase the lateral resolution of imaging and obtain more accurate positioning for the geologic events. At the beginning of the workflow design, the frequency-velocity analysis was

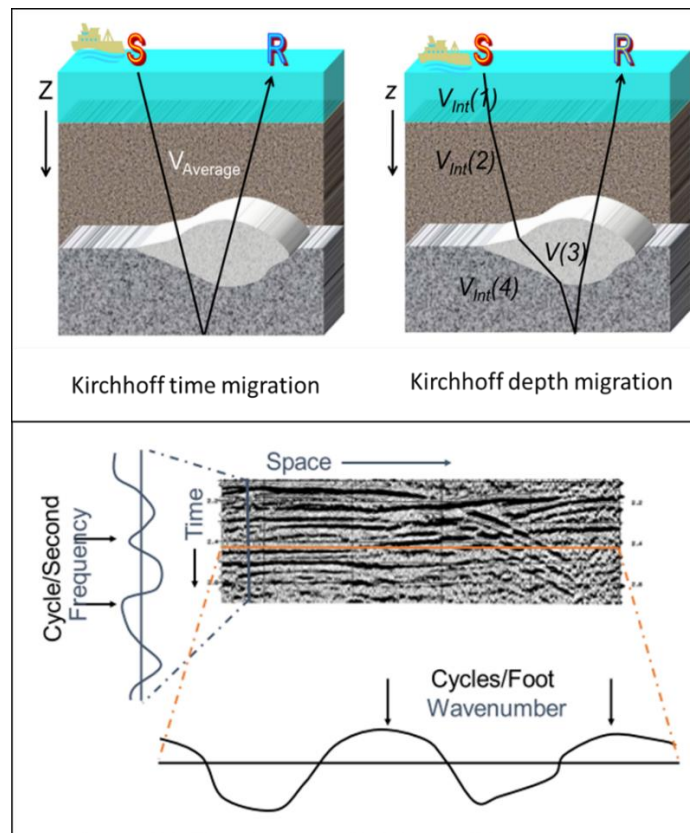
thought to be performed in both domains. Following this purpose, the 3D interval velocity cube (in depth domain) was included in the workflow. Then, this interval velocity cube was converted into the average velocity cube by using an attribute employing Dix's equations. However, since the area of interest covering all the channels studied was found in relatively shallow sections which are not exhibiting significant velocity changes, frequency-velocity relation analysis did not indicate any remarkable variations in the channels. It might be tried for stratigraphic events located at much more different depths from each other in the future.

APPENDICES

Appendix A

Unit and ray-tracing differences between the time and depth seismic data

These figures indicate how rays are travelling differently at the subsurface between the time and depth domains and the unit differences between them. Note that the time-frequency relationship is expressed with cycles/second (Hz) in the time domain whereas it is cycles/foot (wavenumber) in the depth domain. The velocities used for the calculations and migration step are also different. Time-domain accepts average velocities while the depth domain was using interval velocities which is more accurate.

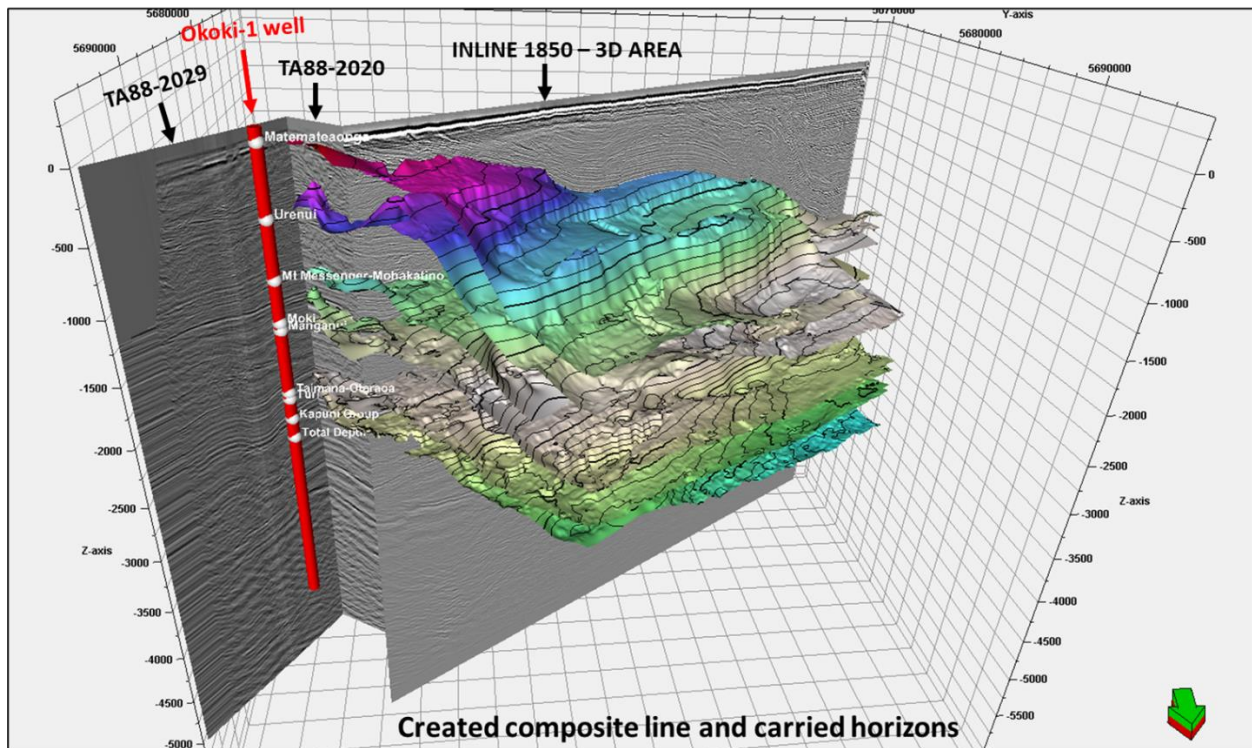


Hill and Rüger, 2019.

Appendix B

3D visualization of the horizons carried along the composite line

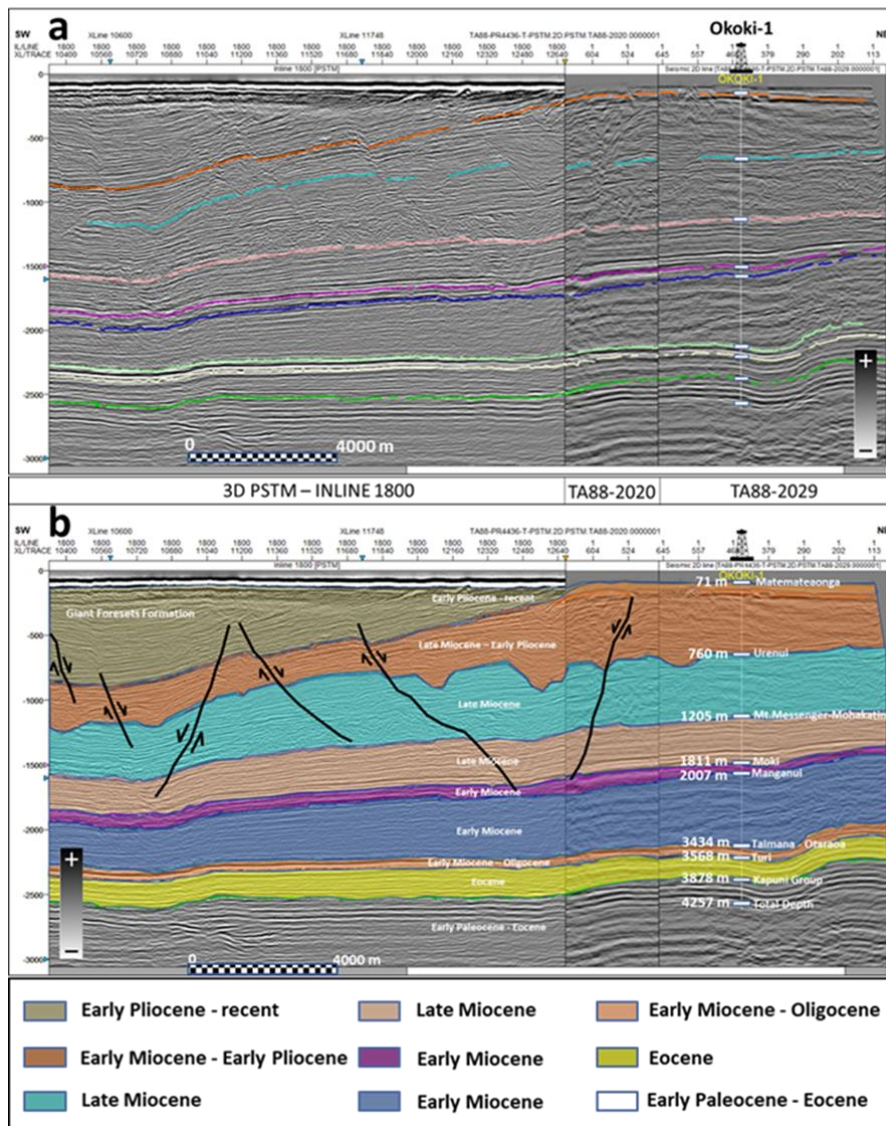
The 3D display below demonstrates the interpreted formation tops and the composite line created to carry the borehole information into the 3D area. Okoki-1 borehole data was tied to the TA88-2029 line, then transferred to TA88-2020 which is perpendicular to it, and finally, all the borehole information was carried into the TORO 3D survey area.



Appendix C

Interpreted and carried horizons on the composite line and modeled version

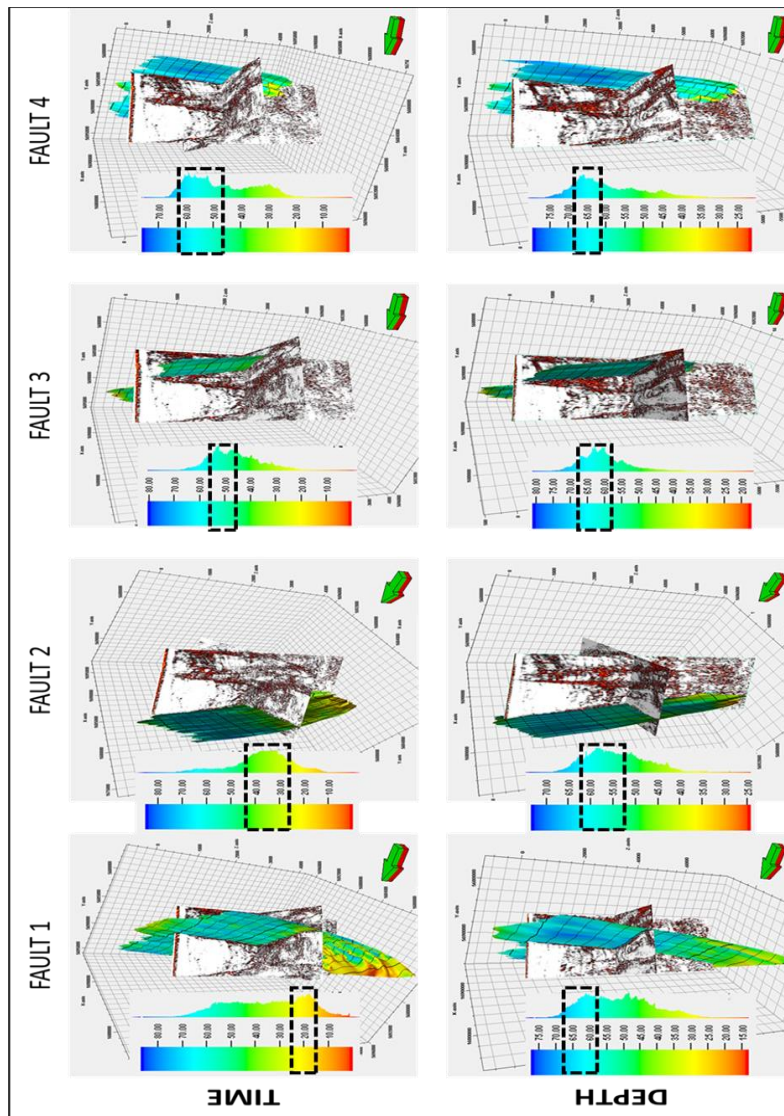
Figure-a shows how the formation tops were carried into the 3D seismic (left side-inline 1800) via a composite line. Figure-b is the modeled version of the interpretation. Note the consistency of the reflections although used two 2D lines and one 3D line. Though the dominant frequencies, velocities, and sample rates are different between the datasets, formation tops were carried successfully from the borehole data into the 3D seismic.



Appendix D

3D visualization of the dip magnitude analysis for each fault

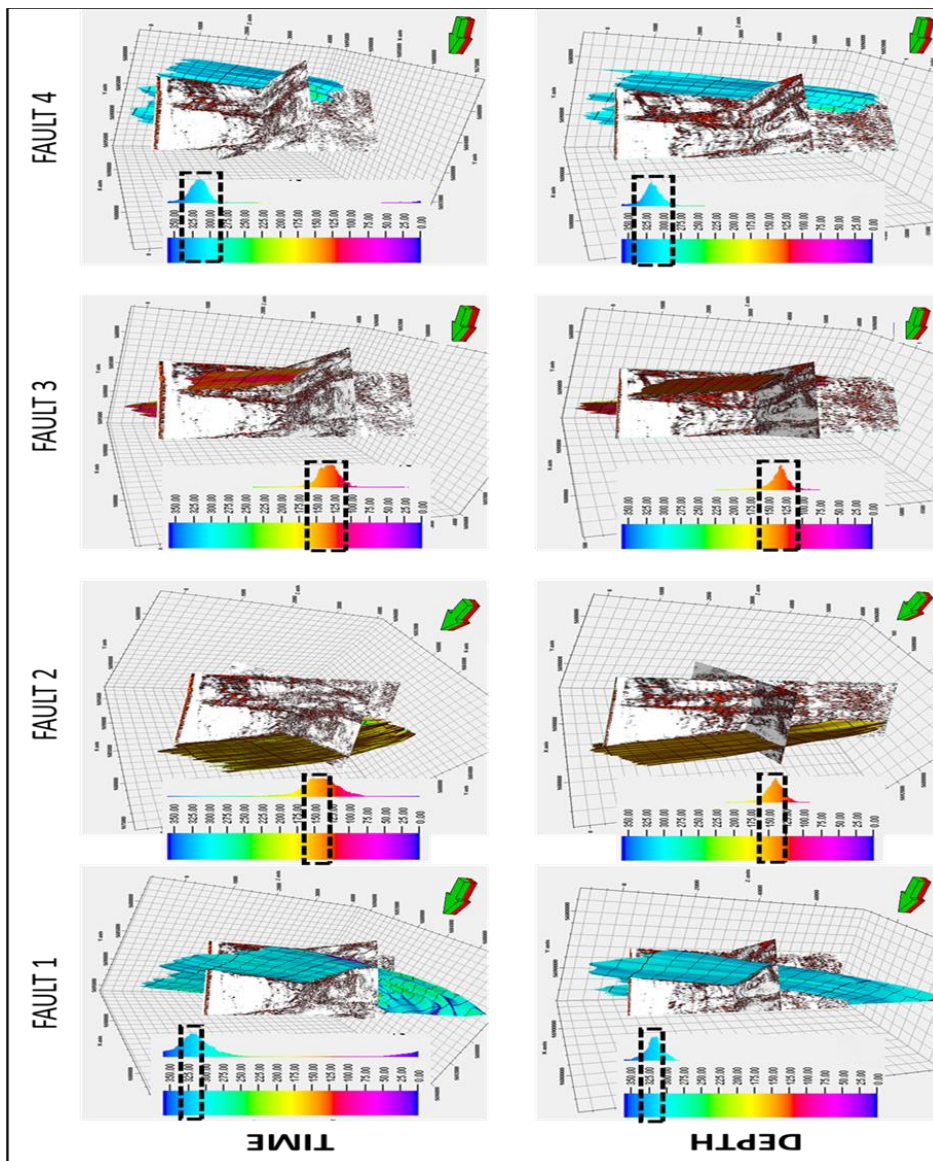
These displays explain the dip angle changes of the analyzed faults in both domains and provide quantitative information rather than only the qualitative point of view shown in the thesis. The 3D visualization of the fault planes was depicted with the variance attribute which is a very useful tool for fault detection. It can be easily observed that fault dips are dramatically increased when we move into the depth migrated data.



Appendix E

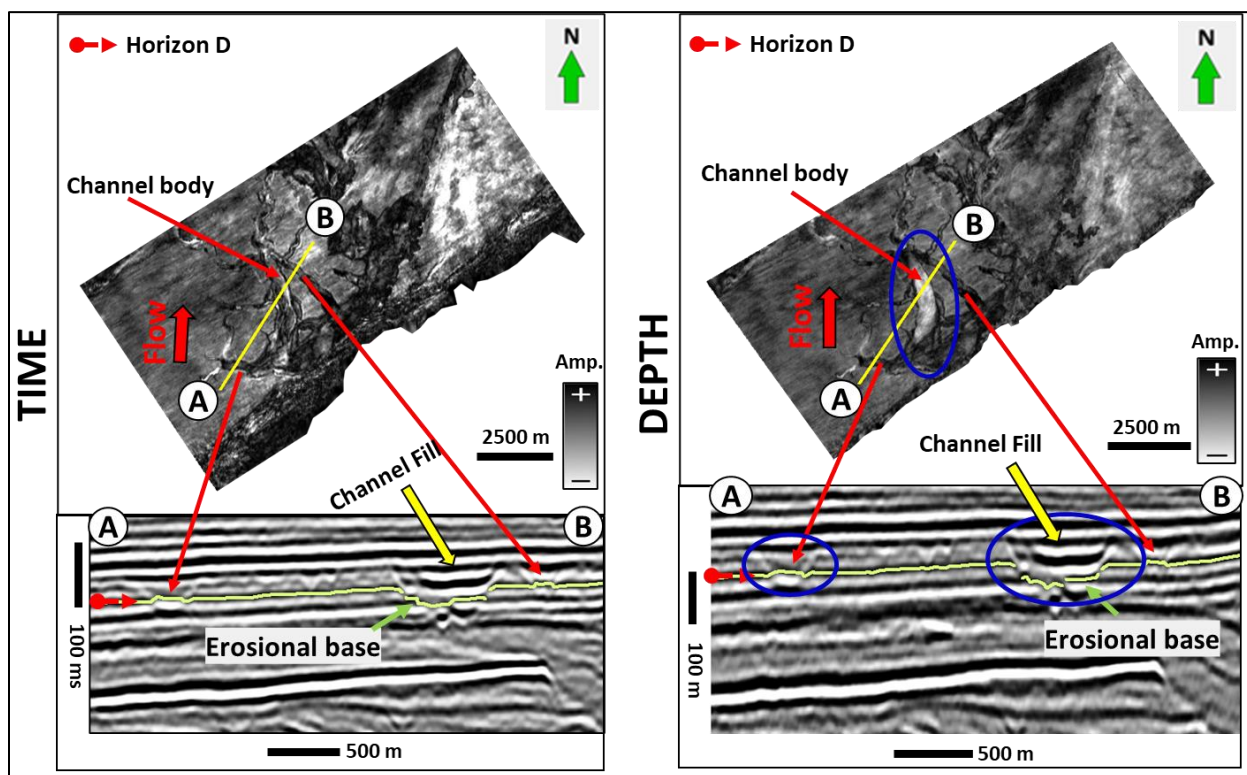
3D visualization of the azimuth analysis for each fault

These 3D displays below indicate the dip azimuth analysis results for each normal fault. Just as explained in the thesis, the depth migration method does not change the direction of the fault planes relative to the north, as a result, we cannot observe remarkable changes in the azimuth angles of the faults.



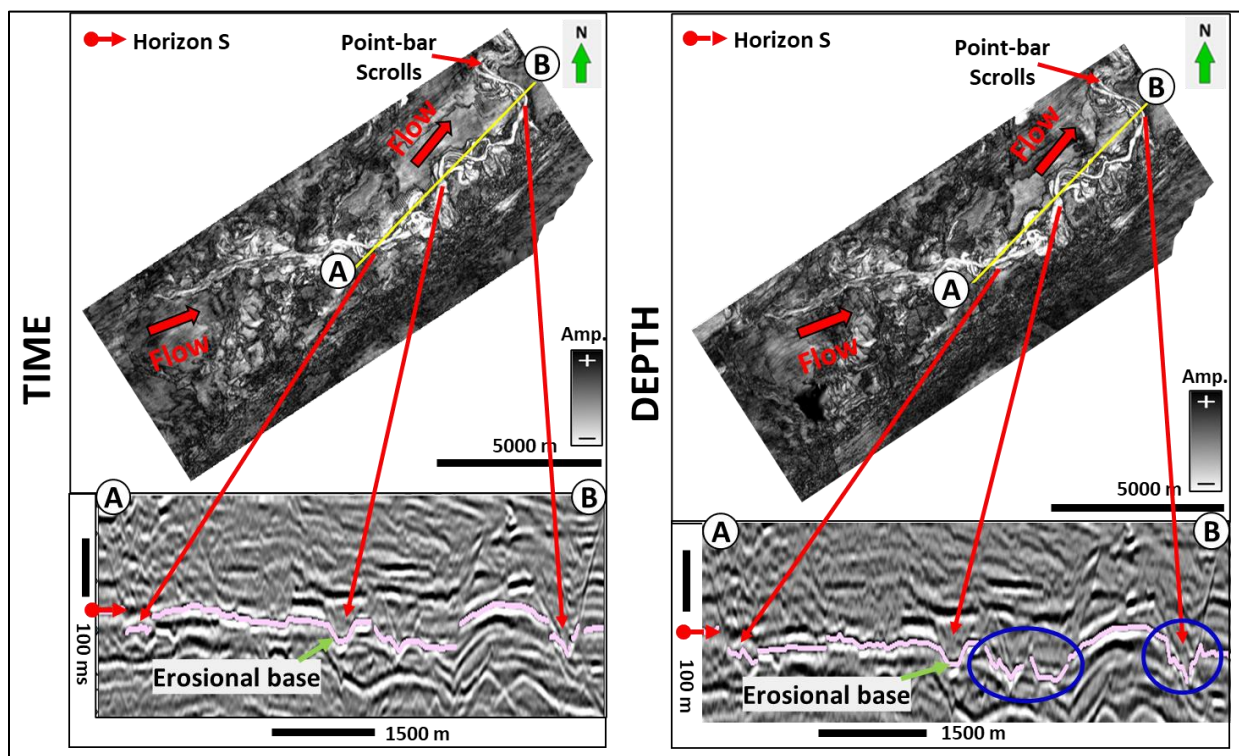
Appendix F

A zoomed display of the distributary channel comparison with horizon slices extracted from the RMS amplitude attribute. There are geometrical (channels are wider and their walls are relatively flatter in the time domain) and also physical (see the amplitude variation inside the main channel body) variations that can be easily detectable between the time and depth migrated datasets. Blue ellipses indicate the variations.



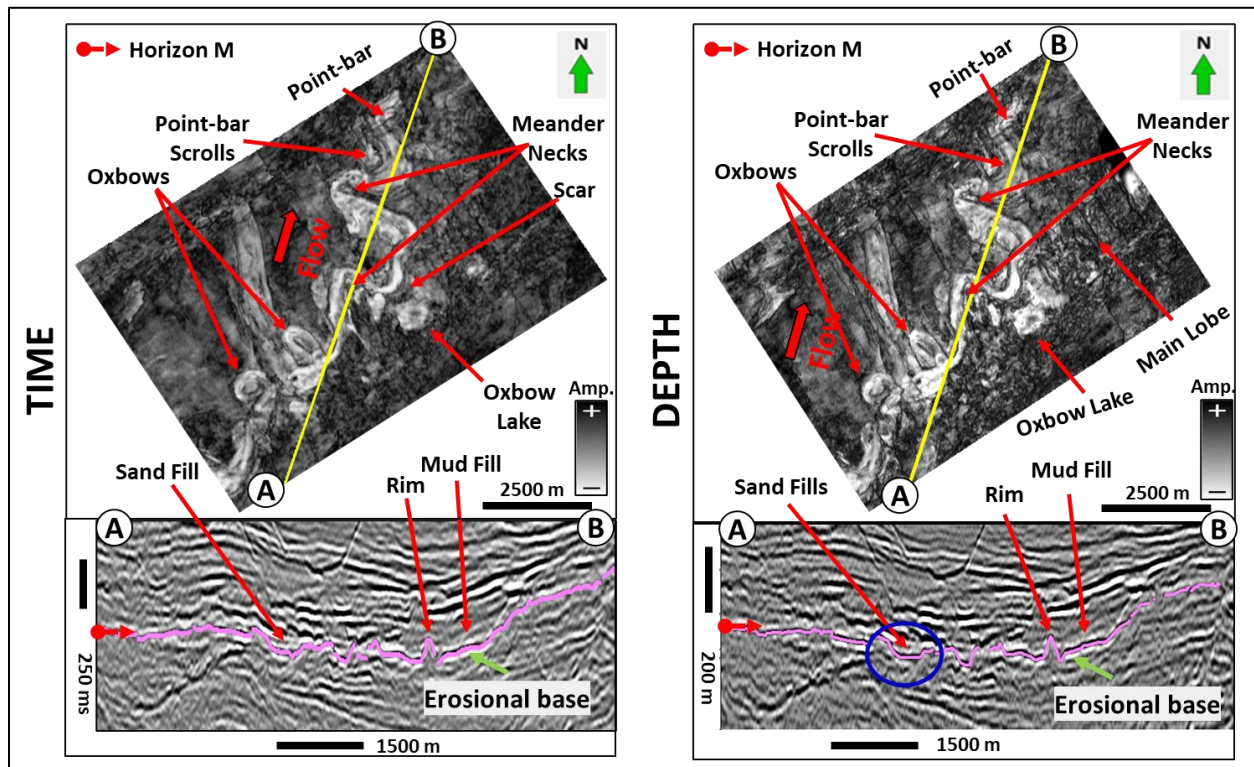
Appendix G

A zoomed display of the sinuous channel comparison with horizon slices extracted from the RMS amplitude attribute. There are geometrical (channel bodies are wider and their walls are relatively flatter in the time domain) variations that can be easily detectable between the time and depth migrated datasets. Blue ellipses indicate the variations.



Appendix H

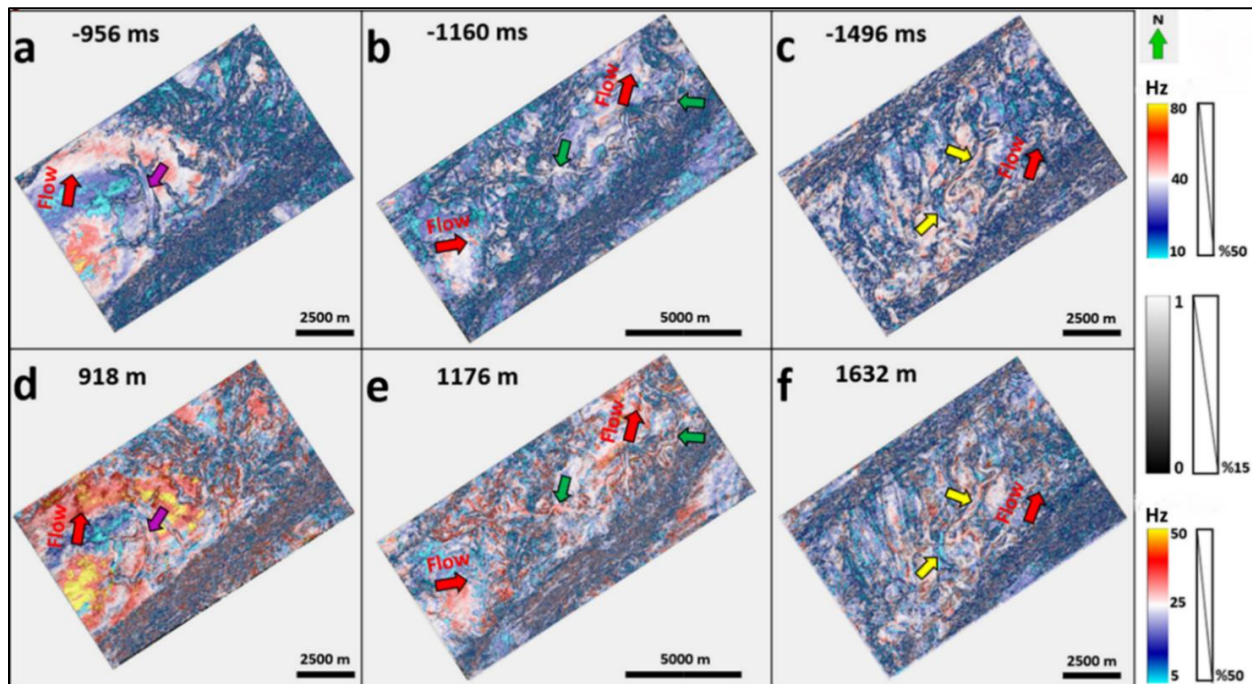
A zoomed display of the meandering channel comparison with horizon slices extracted from the RMS amplitude attribute. There are geometrical (oxbow lakes are narrower and meandering necks are relatively better highlighted in the depth domain) variations that can be easily detectable between the time and depth migrated datasets. Blue ellipses indicate the variations.



Appendix I

Co-rendered instantaneous frequency and the Sobel Filter attribute test

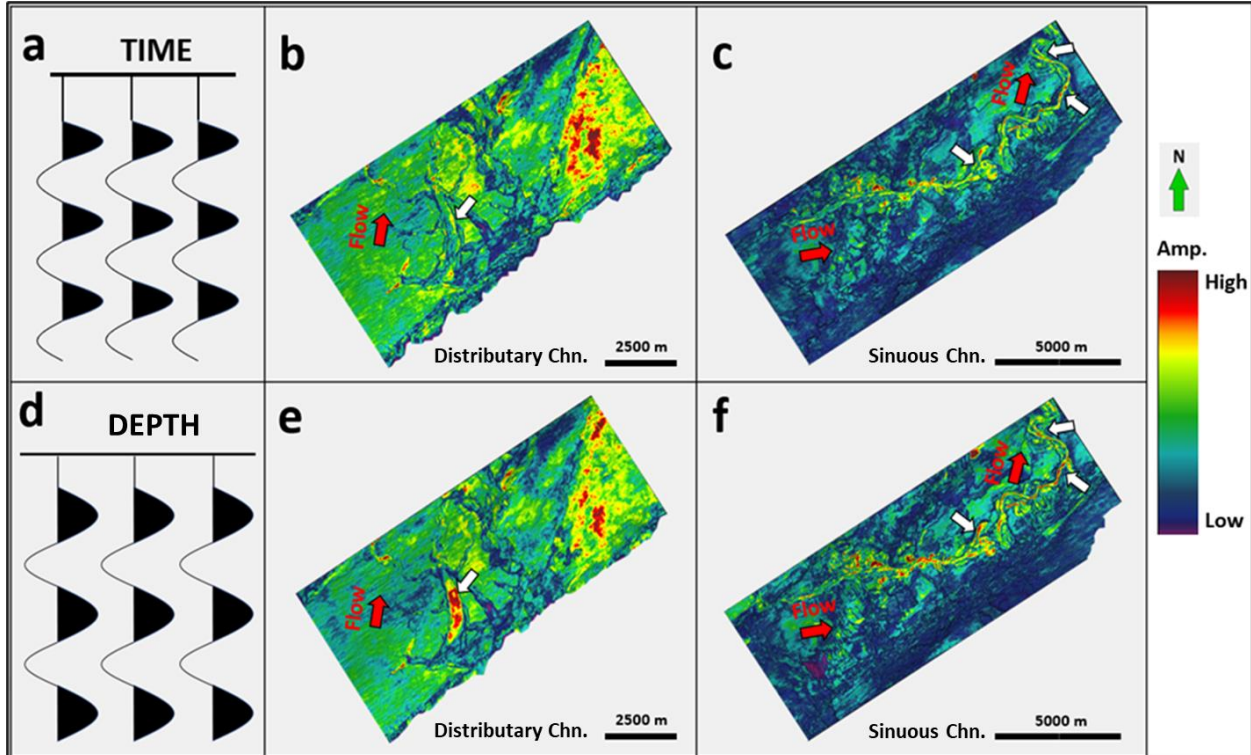
These results below are from the instantaneous frequency attribute displayed by co-rendering with the Sobel Filter similarity attribute. In the time domain, the frequencies range from 0 to 120 Hz whereas they range from 0 to 84 Hz in the depth domain. Remember how we convert the wavenumber (cycles/km) into the Hz (cycles/second). Although the results indicate frequency variations between both domains, we know that these variations can be removed by applying a high-cut filter to the time data. Once they were equated, the frequencies must be almost the same in both domains.



Appendix J

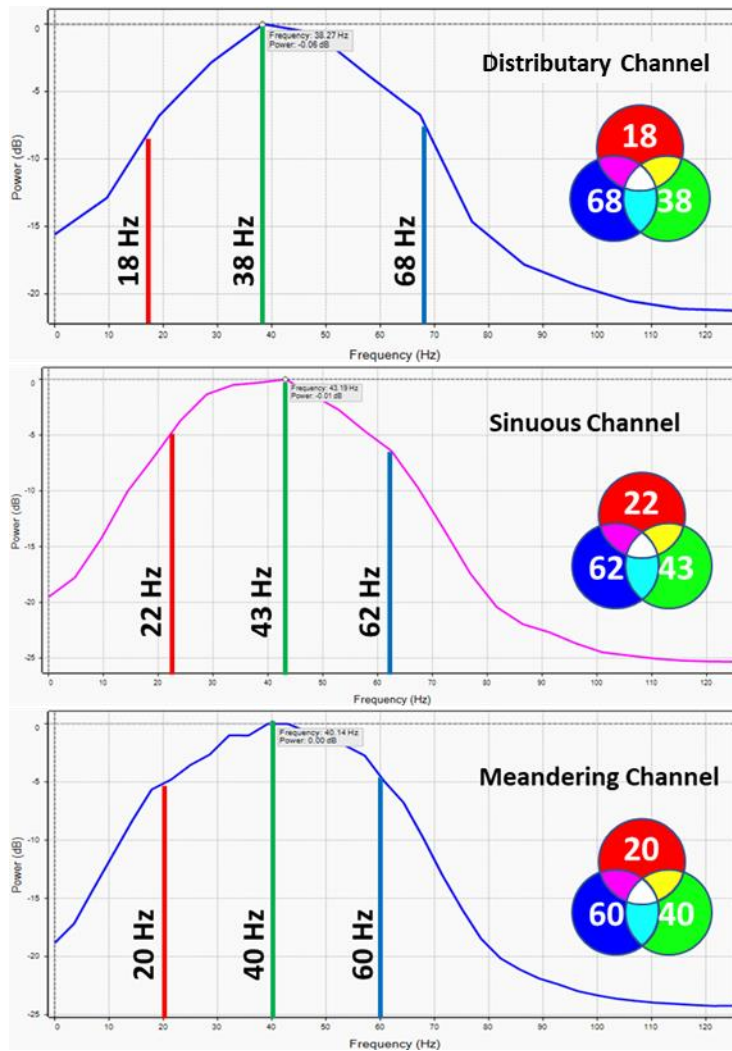
Sweetness attribute test results

The sweetness attribute is derived by dividing reflection strength (envelope) by the square root of instantaneous frequency. It means that any changes in amplitude or frequency will create variations in the results. So, it showed almost the same amplitude variation (white arrows) inside the distributary channel that I observed in the envelope test.



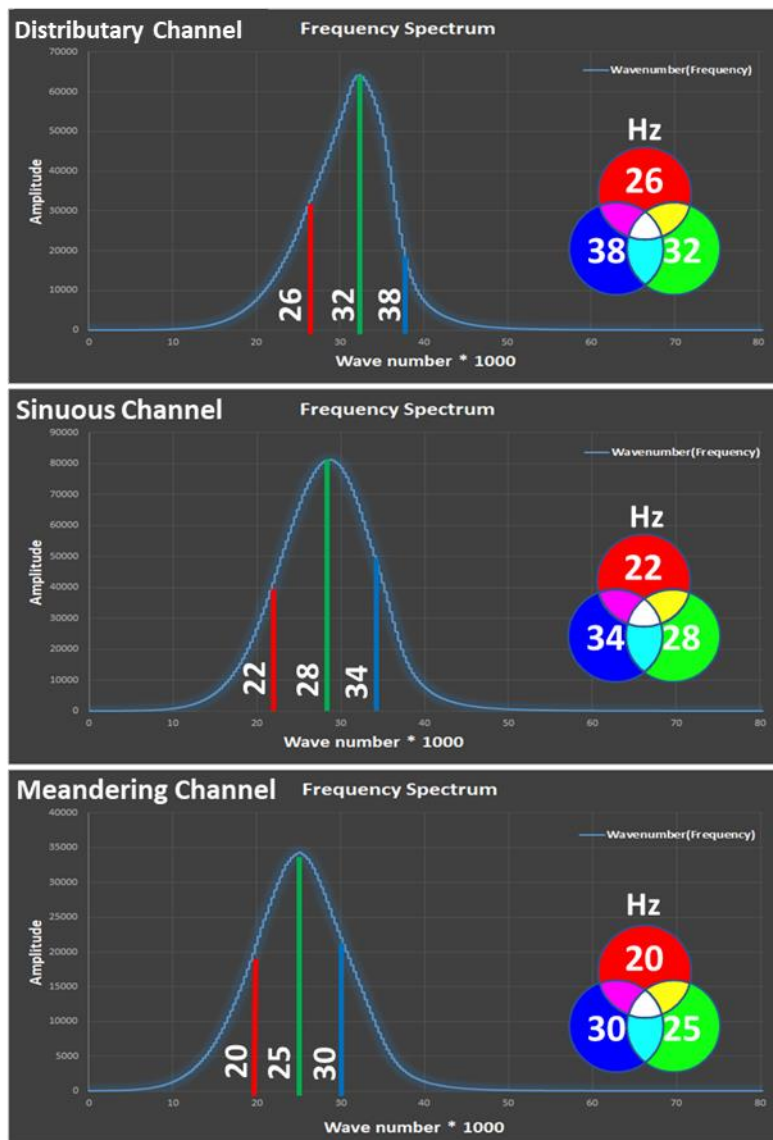
Appendix K

Amplitude-frequency spectrums of the time domain channels used in the spectral decomposition attribute test results



Appendix L

Amplitude-frequency spectrums of the depth domain channels used in the spectral decomposition attribute test results



Appendix M

Filter bank displays showing tuned frequencies for the selected channels used in the multispectral coherence analysis in both domains

The multispectral coherence attribute is an extremely useful tool not only to understand the discontinuities but also to provide information at which frequencies they occur. To perform this attribute is necessary to determine the frequencies to be analyzed before its application. These filter bank displays show the selected frequencies used for the analysis.

Distributary Channel – Time Domain				Distributed Channel – Depth Domain			
F1	F2	F3	F4	F1	F2	F3	F4
8	18	18	28	24	26	26	28
28	38	38	48	30	32	32	34
58	68	68	78	36	38	38	40
Meandering Channel – Time Domain				Meandering Channel – Depth Domain			
F1	F2	F3	F4	F1	F2	F3	F4
10	20	20	30	17.5	20	20	22.5
30	40	40	50	22.5	25	25	27.5
50	60	60	70	27.5	30	30	32.5

Appendix N

Multispectral Coherence attribute test results

To perform this, the energy ratio similarity attribute volume was selected as a coherence part. The RGB blending method results indicate that although there is a frequency range difference between the time and depth migrated datasets, there were not indicate significant variations in the channel edges and faults (marked by the black arrows). The observed variations are caused by the energy ratio similarity attribute which provides a better edge detection in the time migrated data.

